JOURNAL OF GEOPHYSICAL RESEARCH, VOL. 111, A11S11, doi:10.1029/2006JA011700, 2006

Analyzing electric field morphology through data-model comparisons of the Geospace Environment Modeling Inner Magnetosphere/Storm Assessment Challenge events

Michael W. Liemohn,[1] Aaron J. Ridley,[1] Janet U. Kozyra,[1] Dennis L. Gallagher,[2] Michelle F. Thomsen,[3] Michael G. Henderson,[3] Michael H. Denton,[4] Pontus C. Brandt,[5] and Jerry Goldstein[6]

Received 1 March 2006; revised 3 August 2006; accepted 30 August 2006; published 9 November 2006.

[1] The storm time inner magnetospheric electric field morphology and dynamics are assessed by comparing numerical modeling results of the plasmasphere and ring current with many in situ and remote sensing data sets. Two magnetic storms are analyzed, 22 April 2001 and 21–23 October 2001, which are the events selected for the Geospace Environment Modeling (GEM) Inner Magnetosphere/Storms (IM/S) Assessment Challenge (IMSAC). The IMSAC seeks to quantify the accuracy of inner magnetospheric models as well as synthesize our understanding of this region. For each storm, the ring current-atmosphere interaction model (RAM) and the dynamic global core plasma model (DGCPM) were run together with various settings for the large-scale convection electric field and the nightside ionospheric conductance, while keeping all other simulation settings the same. DGCPM plasmaspheric parameters were compared with IMAGE-EUV plasmapause extractions and LANL-MPA plume locations and velocities. RAM parameters were compared with *Dst**, LANL-MPA fluxes and moments, IMAGE-MENA images, and IMAGE-HENA images. Both qualitative and quantitative comparisons were made to determine the electric field morphology that allows the model results to best fit the plasma data at various times during these events. The simulations with self-consistent electric fields were, in general, better than those with prescribed field choices. This indicates that the time-dependent modulation of the inner magnetospheric electric fields by the nightside ionosphere is quite significant for accurate determination of these fields (and their effects). It was determined that a shielded Volland-Stern field description driven by the 3-hour *Kp* index yields accurate results much of the time but can be quite inconsistent. The modified McIlwain field description clearly lagged in overall accuracy compared to the other fields, but matched some data sets (like *Dst**) quite well. The rankings between the simulations varied depending on the storm and the individual data sets, indicating that each field description did well for some place, time, and energy range during the events, as well as doing less well in other places, times, and energies. Several unresolved issues regarding the storm time inner magnetospheric electric field are discussed.

Citation: Liemohn, M. W., A. J. Ridley, J. U. Kozyra, D. L. Gallagher, M. F. Thomsen, M. G. Henderson, M. H. Denton, P. C. Brandt, and J. Goldstein (2006), Analyzing electric field morphology through data-model comparisons of the Geospace Environment Modeling Inner Magnetosphere/Storm Assessment Challenge events, *J. Geophys. Res.*, *111*, A11S11, doi:10.1029/2006JA011700.

1. Introduction

[2] Two critical plasma populations of the inner magnetosphere are the ring current and the plasmasphere. They comprise the bulk of the plasma mass (plasmasphere) and the bulk of the plasma energy (ring current). In what ways are these two populations important? The ring current influences a variety of near-Earth space environment phenomena that impact humanity. For instance, its inflation of the near-Earth magnetic field [e.g., *Parker and Stewart*, 1967; *Tsyganenko*, 2002; *Tsyganenko et al.*, 2003] alters the drift paths of the relativistic electrons in the radiation belts,

[1]Atmospheric, Oceanic, and Space Sciences Department, University of Michigan, Ann Arbor, Michigan, USA.
[2]National Space Science and Technology Center, NASA Marshall Space Flight Center, Huntsville, Alabama, USA.
[3]ISR-1, Los Alamos National Laboratory, Los Alamos, New Mexico, USA.
[4]University of Southampton, Southampton, UK.
[5]Johns Hopkins University Applied Physics Laboratory, Laurel, Maryland, USA.
[6]Southwest Research Institute, San Antonio, Texas, USA.

0148-0227/06/2006JA011700$09.00

causing increased precipitation into the upper atmosphere and influencing the poststorm development of the belts [e.g., *Hudson et al.*, 1998; *Green and Kivelson*, 2001]. Another influence is through the modulation of the near-Earth electric field [e.g., *Jaggi and Wolf*, 1973; *Fok et al.*, 2001]. This alters the subauroral ionospheric wind pattern, augmenting low-density troughs and creating high-density plumes at unexpected times and places, which cause errors in GPS signal processing [e.g., *Yeh et al.*, 1991; *Foster et al.*, 2002].

[3] The plasmasphere also influences a number of space environment phenomena. For example, it is a primary modulator of wave-particle interactions [e.g., *Dungey*, 1963; *Kennel and Petschek*, 1966; *Thorne et al.*, 1973]. The plasmapause, the (often sharp) outer boundary of the plasmasphere [*Carpenter*, 1963], is a critical factor in the location and intensity of plasma waves in the inner magnetosphere [e.g., *Lyons and Williams*, 1984; *Summers et al.*, 1998]. The plasmapause can have some unusual topologies during storms, with the formations of plumes, channels, fingers, and shoulders [e.g., *Carpenter*, 1962; *Park and Carpenter*, 1970; *Chappell et al.*, 1970; *Sandel et al.*, 2003]. In addition, the fate of the eroded plasmaspheric material once it is swept to the dayside magnetopause is largely unknown [*Ober et al.*, 1997a; *Su et al.*, 2000, 2001; *Chandler and Moore*, 2003]. It might recirculate back to the plasma sheet [*Freeman et al.*, 1977; *Borovsky et al.*, 1997; *Elphic et al.*, 1997], which means it could be a crucial supply of particles for subsequent ring current injections.

[4] There are still things we do not know about the stormtime ring current and plasmasphere, especially with regard to the ring current's nonlinear feedback on the electric field. Several recent studies have explicitly compared the accuracy of various electric field models in the inner magnetosphere. *Jordanova et al.* [2001] showed that ring current simulations with the Weimer potential yielded better ion distribution comparisons against data than a Volland-Stern potential. *Boonsiriseth et al.* [2001] found that potentials from the assimilative mapping of ionospheric electrodynamics (AMIE) model [*Richmond and Kamide*, 1988], together with the penetration electric field of *Ridley and Liemohn* [2002], produced excellent agreement with in situ field electric measurements (better than the empirical models considered). *Jordanova et al.* [2003] has now used these electric fields for a storm simulation, showing good agreement with data. Using AMIE potentials in their hot ion transport model, *Chen et al.* [2003] showed that concentrations of potential in narrow channels rapidly transport plasma sheet particles into the inner magnetosphere (a feature not found in simple two-cell models). A similar study by *Khazanov et al.* [2004a] extended these results by including the *Weimer* [1996] electric potential model in the comparison, finding that the morphology of that field description is in between a two-cell pattern and the AMIE fields in their complexity. Furthermore, *Khazanov et al.* [2004b] have shown that a slowly varying AMIE potential pattern is not sufficient for accuracy in the resulting plasma distributions.

[5] *Fok et al.* [2001] showed that a self-consistent electric field produced a pattern significantly different from the standard two-cell morphology, in particular the existence of an extra potential well near local midnight [cf., *Southwood and Wolf*, 1978]. *Fok et al.* [2003] then showed that this midnight potential well is capable of producing a predawn peak in the asymmetric ring current, as observed by satellite-based energetic neutral atom imagers. A follow-on study by *Khazanov et al.* [2003] showed that the potential structure is even more distorted from a two-cell pattern when self-consistent ionospheric conductances are used instead a statistical conductance pattern. In addition, *Liemohn et al.* [2004] showed that the plasmaspheric morphology is better predicted when a self-consistent electric field is included. All of these results are in qualitative agreement with the strong electric fields observed in the inner magnetosphere and subauroral ionosphere during active times [e.g., *Rowland and Wygant*, 1998; *Foster and Vo*, 2002]. *Ebihara et al.* [2004] and *Liemohn et al.* [2005] each examined the effect of ionospheric conductance on ring current development. Both studies found a strong influence, particularly on the details of the inner magnetospheric plasma distribution. *Garner* [2003] conducted numerical experiments of the storm time ring current with a self-consistent electric field description, finding that the formation of intense electric fields in the inner magnetosphere strongly depends on the plasma sheet parameters. *Ebihara et al.* [2005] also found this type of result with self-consistent electric field numerical experiments, noting a nonlinear relationship between plasma sheet density and the resulting ring current intensity.

[6] The discussion above focused on model results, but there are also many recent data analysis studies addressing inner magnetospheric plasma morphology, using in situ data [e.g., *Greenspan and Hamilton*, 2000; *Ganushkina et al.*, 2000; *Friedel et al.*, 2001; *Jorgensen et al.*, 2004; *Lui*, 2003; *Thomsen*, 2004; *Ebihara and Fok*, 2004; *Le et al.*, 2004] and remote sensing data [*Henderson et al.*, 1997; *Grafe*, 1999; *Jorgensen et al.*, 2001; *Reeves and Henderson*, 2001; *Lui et al.*, 2001a, 2001b; *Brandt et al.*, 2002a, 2002b; *Mitchell et al.*, 2003; *Goldstein et al.*, 2002, 2003, 2004, 2005; *Gallagher et al.*, 2005].

[7] Questions still exist about the ring current's influence on the inner magnetospheric electric field and its subsequent feedback on the ring current and plasmasphere. One issue is that the published numerical studies consider just one storm event at a time, and therefore it is difficult to assess whether a given model result is generally applicable beyond the single event being analyzed. Another issue is that the published studies only consider a few data sets for validation and comparison. A final issue is that there is not a comprehensive summary of these published results.

[8] The present study addresses all three of these issues regarding electric field morphology effects on inner magnetospheric plasma dynamics. First, two storm events will be considered, using exactly the same numerical approach and parameter settings to simulate the events. Several simulations are conducted for each storm, varying the large-scale electric field while keeping all other simulation settings the same. Second, numerous data sets will be employed to quantify the accuracy of the simulation results, ranging from localized in situ measurements to remote observations of the inner magnetospheric particle distribution to globally integrated geomagnetic indices. Finally, the

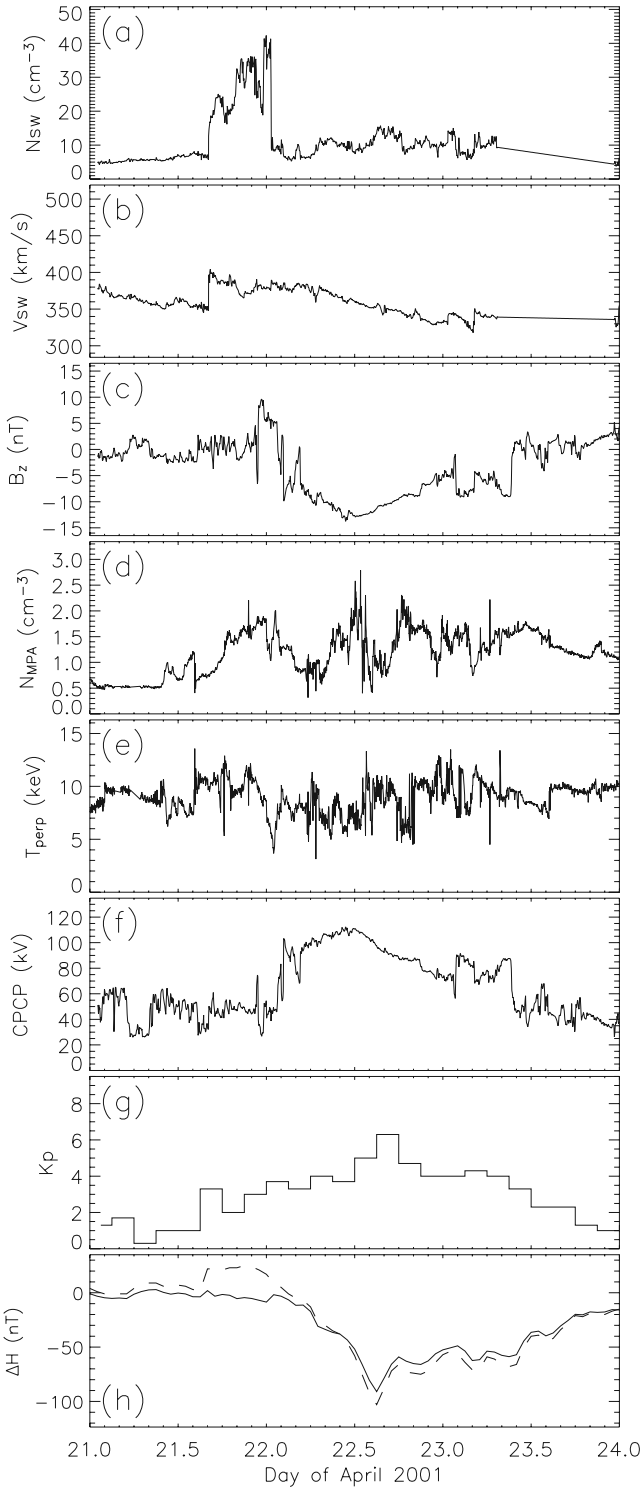

Figure 1. Solar wind, interplanetary magnetic field (IMF), and geophysical parameters for the 22 April 2001 storm (storm 1). Shown are (a) solar wind density, (b) solar wind bulk speed, (c) IMF *Bz*, (d) nightside geosynchronous altitude hot ion density, (e) nightside geosynchronous altitude hot ion perpendicular temperature, (f) cross polar cap potential, (g) the 3-hour *Kp* index, and (h) the 1-hour *Dst* index (dashed line) along with its derivative *Dst** time series (solid line).

results will be placed into the context of previous related studies to synthesize our knowledge on this topic to date.

2. Selected Storms

[9] The two storms selected for this study are those of the Inner Magnetosphere/Storm Assessment Challenge (IMSAC) of the National Science Foundation (NSF) Geospace Environment Modeling (GEM) program. The IMSAC is the culminating activity of the IMS Campaign and has a two-fold purpose: (1) to determine the accuracy of the currently available inner magnetospheric models and (2) to coalesce and synthesize the community's understanding of inner magnetospheric physics. To accomplish these goals, two storms were selected for intensive, community-wide examination, including data analysis efforts as well as modeling studies. The selected events were those on 22 April 2001 and 21–23 October 2001, chosen for a variety of reasons but primarily on the availability of inner magnetospheric particle and field data during the main phase. In the following sections, these two storms will be referred to as storm 1 (April 2001) and storm 2 (October 2001). These two storms are described in detail by many of the other papers in this special section and in previously published reports (e.g., *Goldstein et al.* [2005] for storm 1 and *Denton et al.* [2005b] and *Jordanova and Miyoshi* [2005] for storm 2), so only a brief discussion of the storm time solar wind and geophysical conditions relevant to the present study is given here.

[10] The storm on 22 April 2001 was driven by a well-structured magnetic cloud with a southward axial magnetic field. Figure 1 shows the solar wind and interplanetary magnetic field (IMF) data from the Advanced Composition Explorer (ACE) satellite [*McComas et al.*, 1998; *Smith et al.*, 1998], nightside hot ion density and temperature from the magnetospheric plasma analyzer (MPA) instruments [*Bame et al.*, 1993] on the Los Alamos National Laboratory (LANL) geosynchronous orbit satellites, the cross polar cap potential (CPCP) difference from the *Weimer* [2001] model, along with the geophysical activity indices of *Kp* and *Dst*. Along with *Dst* in Figure 1h, *Dst** is also plotted, using this conversion formula

$$Dst^* = \frac{Dst - D_{MP} + D_Q}{C_{IC}} \tag{1}$$

where the terms being removed from *Dst* are the perturbations from the magnetopause Chapman-Ferraro currents $D_{MP} = 15.5\sqrt{P_{sw}}$ (solar wind dynamic pressure in nPa), a quiet time offset $D_Q = -20$ nT, and the influence of induced currents from the diamagnetic Earth $C_{IC} = 1.3$. Note that this definition, which includes a quite time offset and an induced current correction, allows *Dst** to be less intense than *Dst* (that is, closer to zero). The time interval of the figure is 3 days, showing the data from before the storm sudden commencement (SSC), through the main phase and *Dst* minimum, and well into the late recovery phase. Note that the ACE data has been time delayed by X_{GSM}/Vx_{GSM} throughout this interval.

[11] The shock preceding the cloud did not have a large velocity jump, increasing only about 50 km/s (350 to 400 km/s). The solar wind density is high throughout the

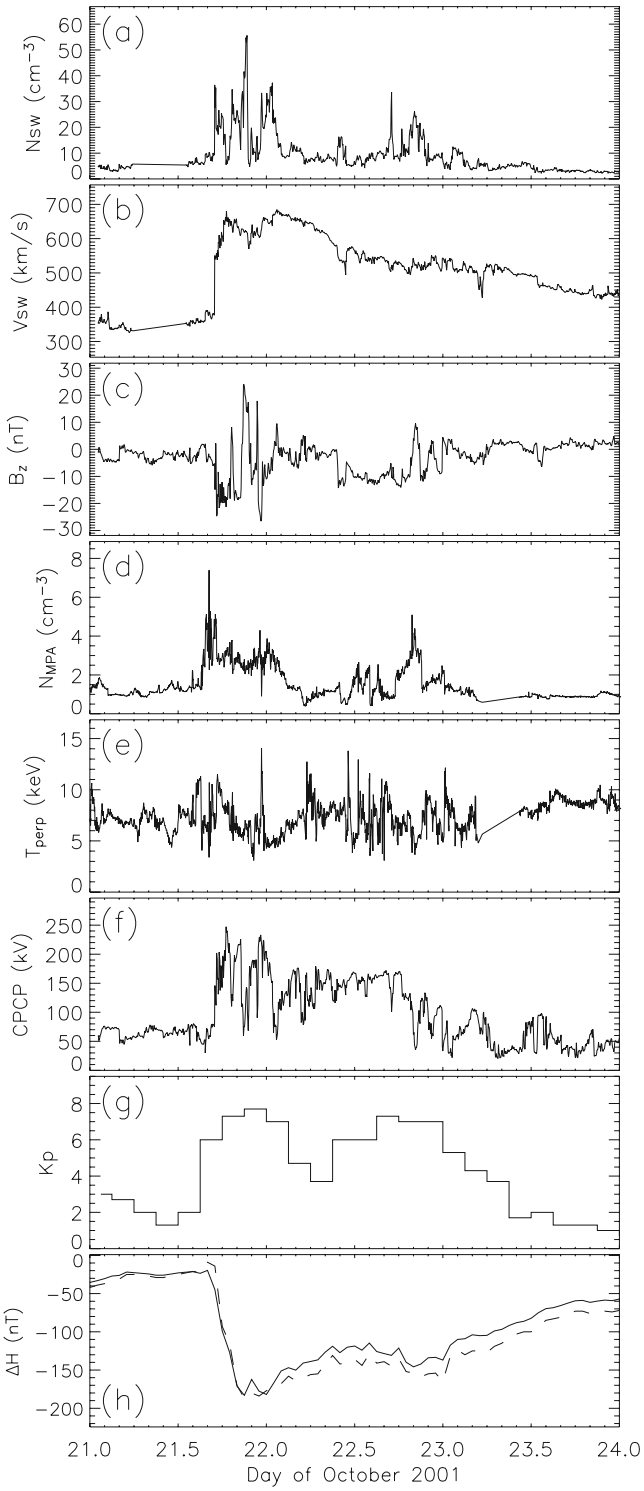

Figure 2. Solar wind, IMF, and geophysical parameters for the 21–23 October 2001 storm (storm 2). The eight panels are the same as those shown in Figure 1.

sheath, varying from 20 to 40 cm^{-3}, but the IMF is either near zero or northward in the sheath. The magnetic cloud contained a southward axial IMF and so the geomagnetic activity level remained high throughout the entire cloud passage. The peak southward IMF reached −13 nT just before noon on 22 April. The resulting storm main phase was long, extending from 2000 UT on 21 April (beginning of the SSC) until 1500 UT on 22 April (*Dst* minimum). The resulting storm was relatively moderate, however, with a *Dst* minimum value of −102 nT, recovering to half this magnitude by the end of the day and to its prestorm level by the end of 23 April. The near-Earth plasma sheet density (Figure 1d) rose to values between 1 and 2 cm^{-3} throughout the storm interval, with spikes up to 3 cm^{-3}. The cross polar cap potential (CPCP) did not rise during the sheath passage, remaining at its prestorm level of roughly 50 kV. During the cloud passage, the CPCP rose to 110 kV. Note that there is a solar wind plasma data gap on 23 April, but this is past the storm peak and does not influence the results and conclusions of this study.

[12] The second event was far more intense than the first, and is, in fact, a multiple-peak storm. Figure 2 shows solar wind moments, IMF *Bz*, nightside geosynchronous plasma moments, CPCP, *Kp*, and *Dst* for the 21–23 October 2001 storm interval. A large shock (Vsw jumped roughly 300 km/s up to a peak of almost 700 km/s) struck the magnetosphere around 1600 UT on 21 October and, after a brief SSC, *Dst* plunged to −187 nT by 2100 UT that day. This initial main phase was caused by the passage of a sheath region in front of a fast-moving magnetic cloud. The sheath contained large IMF *Bz* excursions to ±25 nT. During this interval, the near-Earth plasma sheet density exceeded 4 cm^{-3} (with a short-lived spike beyond 7 cm^{-3}) and the CPCP was often above 200 kV. The cloud had a south-to-north IMF orientation, and its passage by Earth lasted throughout 22 October. *Dst* recovered during the first half of that day, when the IMF was northward or near zero. Upon the IMF's sudden southward turning, *Dst* began to drop again to a second *Dst* minimum of −165 nT at 0000 UT on 23 October. There was an initial rapid recovery of *Dst* for a couple of hours, followed by a slower return toward zero. *Dst* was still quite depressed 24 hours (around −70 nT) and 48 hours (around −40 nT) after the second peak. *Kp* shows a similar double peak (8− and 7+), with a deeper relative minimum between them (4−) than is seen in the *Dst* index.

[13] A major similarity between the two storms is that they are almost exactly 6 months apart, so the absolute value of the Earth's tilt angle is the same. Therefore the difference in hemispheric illumination is the same for the two events (although flipped). Another similarity is that they were both driven by magnetic clouds (although the October event also had a highly geoeffective sheath region preceding the cloud).

[14] A major difference between the two events is the intensity; storm 2 is nearly double the size of storm 1 in terms of *Dst* minimum value. This is also seen in the MPA and CPCP values; the nightside hot ions are twice as dense and the large-scale convection is nearly twice as strong. Another big difference is that the second storm is a double-dip event, with the sheath and the cloud producing large magnetic storms in geospace. A third difference is the rapidness of the main phase development, which was very slow (less than 5 nT/h average drop in *Dst*) in storm 1 but very fast in storm 2 (average drop of over 40 nT/h).

[15] These similarities and differences offer a variety of opportunities for addressing the goals of the IMSAC, and in particular the issue to be addressed in this study. That is, from the similarities and differences in the driver conditions

and geophysical responses between these two storms, new information about the inner magnetospheric electric field morphology and dynamics can be discerned and existing ideas can be validated (or challenged, as we will see).

3. Technical Approach

[16] To quantitatively examine the influence of electric field morphology on the dynamics of plasma in the inner magnetosphere, several simulations will be conducted for the two storms. For each storm, the large-scale electric field is specified differently between the simulations while keeping all other inputs and boundary conditions the same. The simulation results are then compared against numerous data sets in a robust assessment of their strengths and weaknesses. This section describes the numerical model used for the study, the basic features of the inner magnetospheric electric potentials from the various descriptions for each storm, and the data-model comparison technique.

3.1. Model

[17] The ring current-atmosphere interaction model (RAM) described by *Liemohn et al.* [2004, 2005] was used for this study. This version of RAM, based on earlier versions by *Fok et al.* [1993], *Jordanova et al.* [1996], and *Liemohn et al.* [1999], solves the time-dependent, gyration- and bounce-averaged kinetic equation for the phase-space density $f(t, R, \varphi, E, \mu_0)$ of one or more ring current species (H^+ and O^+ for this study):

$$\frac{\partial f^*}{\partial t}+\frac{\partial}{\partial \vec{R}_\perp}\left\{\left\langle\frac{d\vec{R}_\perp}{dt}_{\vec{E}}\right\rangle f^*\right\}+\frac{\partial}{\partial E}\left\{\left\langle\frac{dE}{dt}_{\vec{E}}\right\rangle f^*\right\}+\frac{\partial}{\partial \mu_0}\left\{\left\langle\frac{d\mu_0}{dt}_{\vec{E}}\right\rangle f^*\right\}=\frac{\partial}{\partial E}\left\{\left\langle\frac{dE}{dt}_{CC}\right\rangle f^*\right\}+\frac{\partial}{\partial \mu_0}\left\{\langle D_{CC}\rangle\frac{\partial f^*}{\partial \mu_0}\right\}-\frac{f^*}{\tau_{CE}}-\frac{H(\mu_0-\mu_{0,LC})f^*}{0.5\tau_b} \quad (2)$$

Note that f is related to f^* by a variable-dependent multiplier,

$$f=\frac{f^*}{R_0^2\mu_0 h(\mu_0)\sqrt{E}} \quad (3)$$

needed for conversion to this conservative form of the kinetic equation [*Jordanova et al.*, 1994, 1996]. The five independent variables are, in order, time, geocentric distance in the equatorial plane (in units of R_E), magnetic local time ($\varphi = 0$ at midnight, increasing eastward), kinetic energy (in keV), and cosine of the equatorial pitch angle. In (3), $h(\mu_0)$ is a bounce-averaging integral [e.g., *Ejiri*, 1978].

[18] The code includes collisionless drifts (left-hand side of (2)), energy loss and pitch angle scattering due to Coulomb collisions with the thermal plasma (first two terms on the right-hand side of (2), with cold plasma densities from the *Ober et al.* [1997b] model), charge exchange loss with the hydrogen geocorona (third term on the right-hand side of (2), with H densities from the *Rairden et al.* [1986] model), and precipitative loss to the upper atmosphere (last term in (2)). Second-order accurate, finite volume, numerical operators are used to obtain f in several million grid cells throughout velocity and configuration space in the inner magnetosphere, covering the energy range from 10 eV to 400 keV, L range from 2 to 6.5, and all pitch angles and local times. RAM's typical time step is 10 s for the hot ion simulations. The source term for the phase space density calculated by RAM is the outer simulation boundary, where observed particle fluxes from MPA and the synchronously orbiting particle analyzer (SOPA) [*Belian et al.*, 1992] instruments on the LANL geosynchronous-orbit satellites are applied as input functions. The composition of the inner plasma sheet is assumed to vary with solar and magnetic activity according to the statistical relationship derived by *Young et al.* [1982] (see *Liemohn et al.* [1999] for the applied method). The magnetic field is assumed to be a static dipole. Additional details of the present model development of this version of RAM are presented by *Liemohn et al.* [1999, 2001a, 2004, 2005].

[19] Several electric field descriptions are used in this study. Specifically, this study is focused on determining the improvements to simulating the storm time ring current and plasmasphere over the course of the GEM IMS campaign (a secondary goal of the IMSAC). Therefore four simulations are conducted for each of the two storms. Two of the simulations represent the state of RAM at the beginning of the IMS campaign: the empirically derived formulas of the Volland-Stern electric field description [*Volland*, 1973; *Stern*, 1975; *Maynard and Chen*, 1975; *Jordanova et al.*, 1996] and the modified McIlwain E5D model [*McIlwain*, 1986; *Liemohn et al.*, 2001a]. The Volland-Stern field is controlled by the 3-hour *Kp* index, with a shielding factor of $\gamma = 2$ (a reasonable value, as determined by *Korth et al.* [1999]). The modified McIlwain field is controlled by the Weimer-model-generated CPCP time series as well as the DMSP-derived midnight boundary index [*Gussenhoven et al.*, 1981, 1983], as discussed by *Liemohn et al.* [2001a]. The other two simulations, representing the present state-of-the-art configuration of RAM, employ the self-consistent electric field determination method described by *Liemohn et al.* [2004, 2005]. That is, field-aligned currents (FACs) calculated from the hot ion results [*Liemohn et al.*, 2001b] are used as a source term in the Ridley Ionosphere Model (RIM), a Poisson equation solution for the ionospheric potential [*Ridley and Liemohn*, 2002; *Ridley et al.*, 2004]. Note that the ionospheric auroral zone conductance region, assumed to be a smooth but asymmetric oval, varies in both time and space with the dynamics of the RAM-calculated FACs. The difference between the two self-consistent simulations is the relationship between the peak FAC value and the peak auroral conductance value; one simulation (the "enhanced" self-consistent simulation) has double the conductance of the other simulation (the "nominal" self-consistent simulation). The exact settings for the nominal case are the same as those for the nominal case in the work of *Liemohn et al.* [2004, 2005].

[20] Note that other studies have compared the results of these kinds of electric field models for the plasmasphere [e.g., *Liemohn et al.*, 2004], for the ring current [e.g., *Jordanova et al.*, 2001; *Khazanov et al.*, 2003], and for both [*Liemohn et al.*, 2005]. The results of this study will be put into the context of these earlier studies in section 7 below.

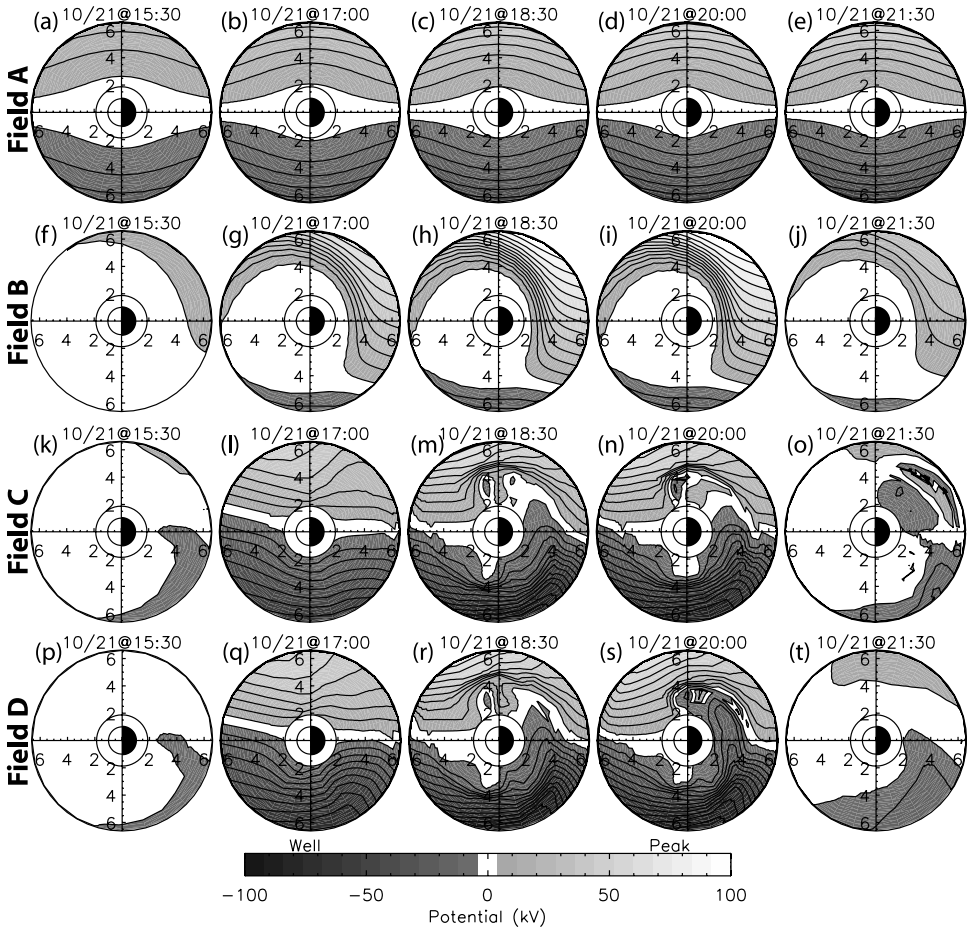

Figure 3. Convection electric potential contours for the four field descriptions during the first main phase of the October 2001 storm. (a)–(e) Field A patterns, (f)–(j) field B patterns, (k)–(o) field C patterns, and (p)–(t) field D patterns. Lighter shading indicates positive potential values, darker shading indicates negative values, and white shading is assigned to the contour level near zero potential. Equipotential lines are drawn every 8 kV (these are also the grayscale shading intervals). The view is over the North Pole with the Sun to the left and distances given in R_E.

[21] The storm time simulation results to be presented below represent an examination of the influence of the inner magnetospheric electric fields on the ring current and plasmasphere. The only variation between the simulations is the electric field description; the magnetic field, the initial conditions, and the boundary conditions are all the same between the various model runs. In the following sections, these four simulation setups will be referred to as field A (Volland-Stern), field B (modified McIlwain), field C (nominal self-consistent), and field D (enhanced self-consistent). Therefore combining this naming system with storm 1 and storm 2 definitions above, the text refers to runs 1A, 1B, 2A, etc., for the eight simulations to be discussed in this study.

3.2. Electric Potential Patterns

[22] Before beginning the presentation of the data-model comparisons, it is useful to point out the main features of the four electric field descriptions. Figure 3 presents illustrative electric potential contour plots in the inner magnetosphere for each model. The plots are all from the first main phase of storm 2, where there was a sudden increase in convection and a rapid buildup of the ring current. Five times are shown (the five columns), with the first time before the SSC, the middle three times during the main phase late on 21 October, and the last time during a brief lull in convection just after the *Dst** minimum. Lighter shades of gray indicate positive potentials, darker shades are for negative potentials, with the bin surrounding zero potential set to white. The contours are spaced 8 kV apart. Note that the corotation potential has not been added to these contour plots; only the convection electric potential is shown in Figure 3.

[23] It is seen that the *Kp*-driven Volland-Stern field (field A, Figures 3a–3e) does not change much. The morphology is static, and only the intensity varies with time (doubling over this interval). Note that convection is already elevated at 1500 UT because of the 3-hour cadence of Kp. The shielding function of this field is seen by the slight deflection of the potential contours around Earth.

[24] The modified McIlwain field (field B, Figures 3f–3j) also has a relatively fixed morphology. The shielding parameter varies with time according to the midnight auroral boundary index, which has a 5 to 20 min cadence. Because the intensity is driven by the Weimer potential

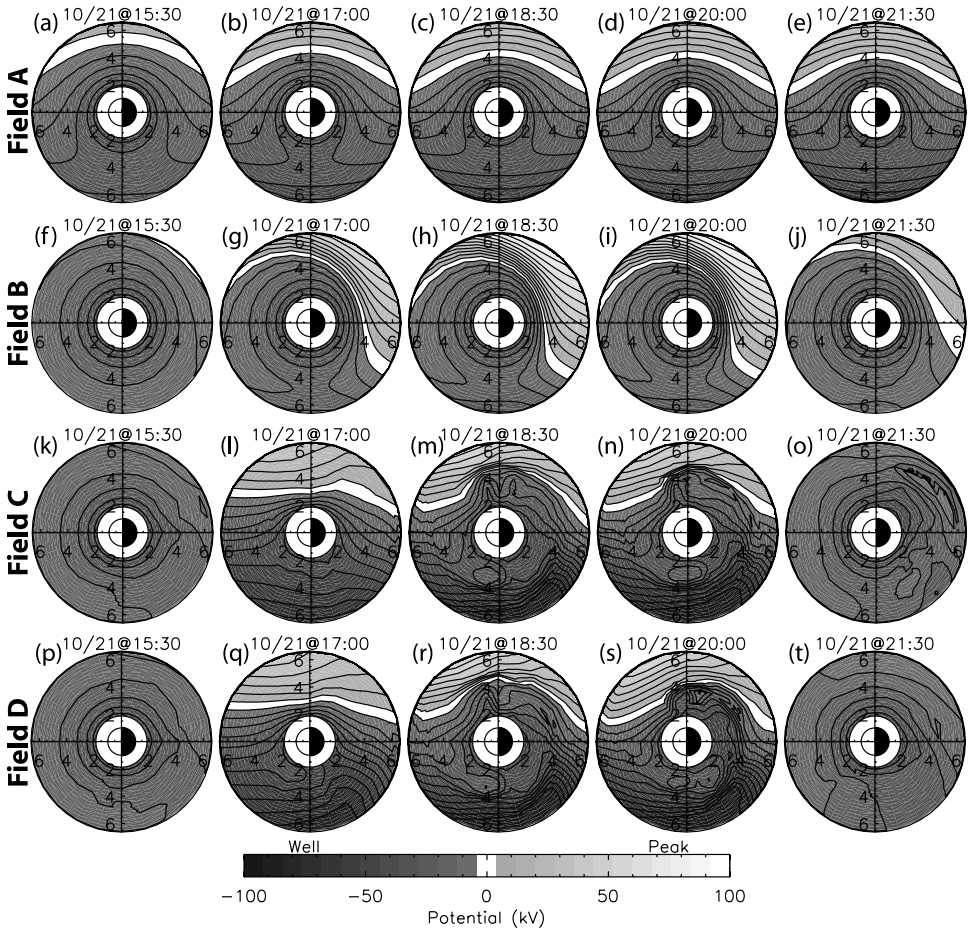

Figure 4. Electric potential contours with both convection and corotation included for the four field descriptions during the first main phase of the October 2001 storm. The format and color scale are the same as in Figure 3.

pattern at high latitudes, convection increases after the SSC and noticeably decreases after the storm peak. Two unique features of this field description are (1) the strong potential gradient near dawn and (2) the weak potential gradient across the dayside, especially in the afternoon sector.

[25] The nominal self-consistent field (field C, Figures 3k–3o) exhibits a highly dynamic morphology. Figure 3k is very quiet with a small midnight potential well from a weak plasma injection an hour earlier. The beginning of the main phase (Figure 3l) reveals almost no inner magnetospheric shielding of the strong convection potential. Later in the main phase (Figures 3m and 3n), a midnight potential well has been reestablished, and small-scale relative pressure extrema produce local peaks and valleys in the electric potential [e.g., *Liemohn and Brandt*, 2005]. Around dusk, a strong potential gradient is formed as the potential contours are diverted around a local maximum. The resulting outward electric field creates the phenomenon known as subauroral polarization stream (SAPS) in the midlatitude ionosphere. The midnight well and the dusk peak are formed by upward and downward (respectively) flowing field-aligned currents associated with the closure of the partial ring current. After the main phase, the large-scale convection rapidly decreases, leaving a premidnight potential well (the standard potential structure of overshielding).

[26] The plots for the enhanced self-consistent field (field D, Figures 3p–3t) are quite similar to the patterns for field C, discussed above. There are two main differences to point out, however. The first is the larger midnight potential well in Figure 3s (compared to that in Figure 3n). This is because the enhanced ionospheric conductance decreases the inner magnetospheric shielding potential for a given FAC intensity, and therefore more plasma sheet particles enter the ring current region near Earth. The second difference is that the overshielding potential in the premidnight sector is much weaker in Figure 3t that in Figure 3o. This is because the larger conductances dissipate the current more effectively, resulting in smaller and shorter lived electric fields.

[27] While these plots are useful for understanding the morphology of the convection electric field descriptions, they do not represent the full electric potential in the inner magnetosphere. For that, the corotation potential must be included. It is defined as a potential specifying an electric field such that $\mathbf{E} \times \mathbf{B}$ yields a 24-hour eastward drift period around the Earth (regardless of radial distance). A simple form of this potential is C/R_0, where $C = -91.7$ kV R_E and R_0 is the radial distance in the equatorial plane of a given field line (as defined above). Figure 4 shows the convection potentials of Figure 3 with this corotation potential added in to the values. The equipotential contours in Figure 4 are the

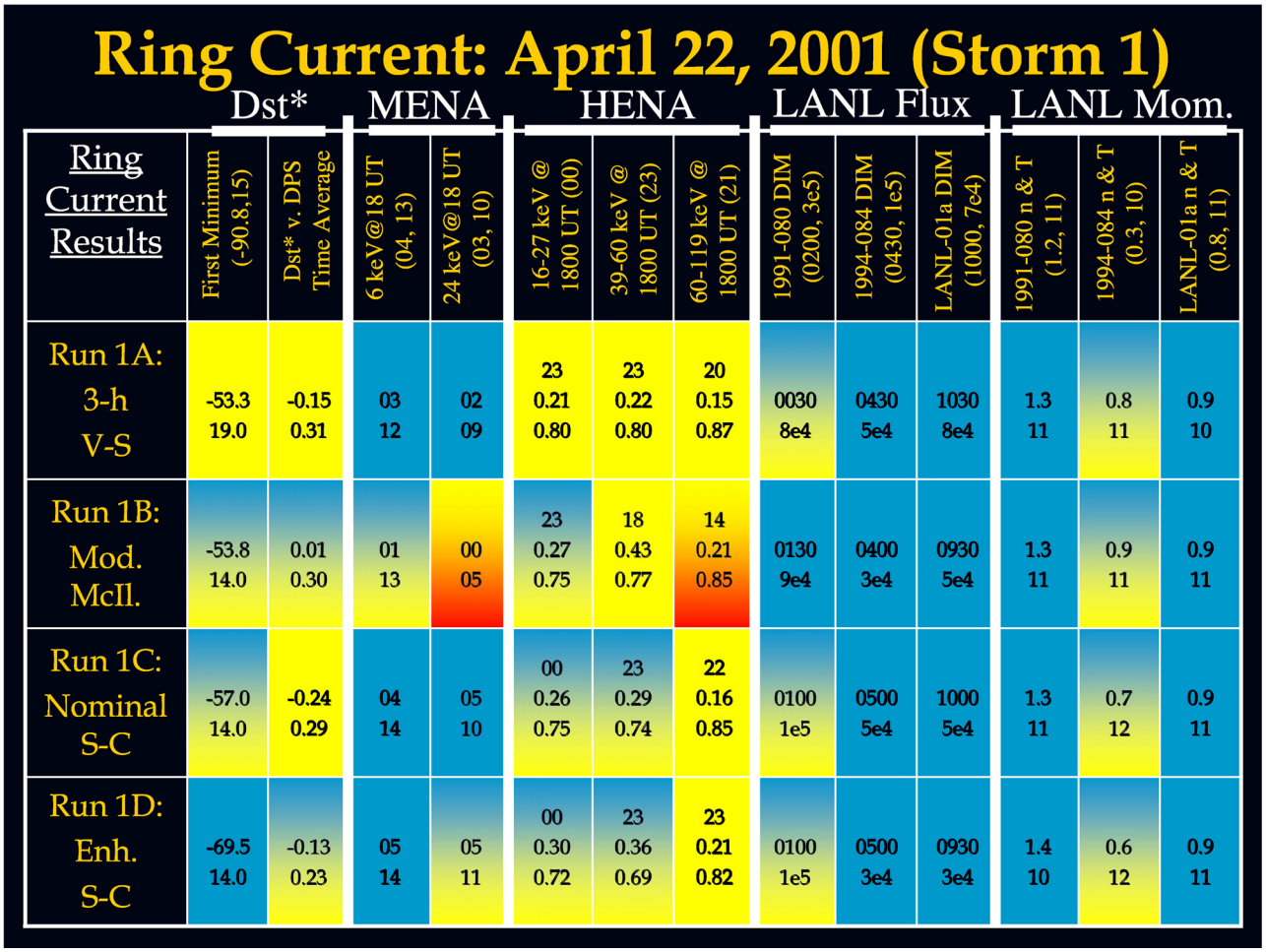

Figure 5. Quantitative assessments of ring current data-model comparisons for the April 2001 storm. The four rows give the results for the four simulations for this storm, while each of the 13 columns are for a different data set (in order: *Dst**, MENA, HENA, LANL fluxes, and LANL moments). Color assignments for each block are made according to the accuracy levels specified in Table 1. Numbers in the column headers are data-derived quantities, for comparison with the values in the column boxes.

instantaneous drift paths of the zero-energy particles in each field description at the selected times. Near the Earth, the corotation potential dominates the distribution, resulting in eastward drifts. Farther out, the convection field dominates and the patterns resemble those of Figure 3. Note that most of the small-scale structure is still evident in the patterns for fields C and D.

[28] With these potential patterns in mind, let us now turn to the individual data-model comparisons for the plasma in the inner magnetosphere. This will allow us to assess the effect of each of these electric field descriptions on the plasmasphere and ring current as well as assess the accuracy of each of these descriptions (as a function of location and time).

3.3. Data-Model Comparison Technique

[29] Coupled RAM-DGCPM simulations were conducted for the two storms with the four different electric field descriptions. These were then compared against numerous data sets in order to quantify the accuracy of the resulting inner magnetospheric plasma distributions. In total, 26 different data-model comparisons are made for each simulation of each storm. In the sections that follow, summary plots are shown of this assessment, with only a few illustrative data-model comparison plots. The individual data and model figures from which the quantitative comparisons were extracted are available as auxiliary material.[1] The electronic supplements for this article include 46 figures, essentially one for each column in Figures 5–8, and a readme text file describing the contents of each of these individual data-model comparison figures.

[30] Let us explain each of the data-model comparisons conducted for this study. The first selected data set is the observed *Dst** time series, which is compared against a simulated version of this number, Dst^*_{DPS} [*Dessler and Parker*, 1959; *Sckopke*, 1966],

$$Dst_{DPS}^*[\mathrm{nT}] = 3.98 \cdot 10^{-30} E_{RC}[\mathrm{keV}] \quad (4)$$

Dst^*_{DPS} linearly relates the magnetic perturbation at the center of the Earth (a proxy for the globally averaged

[1] Auxiliary materials are available in the HTML. doi:10.1029/2006JA011700.

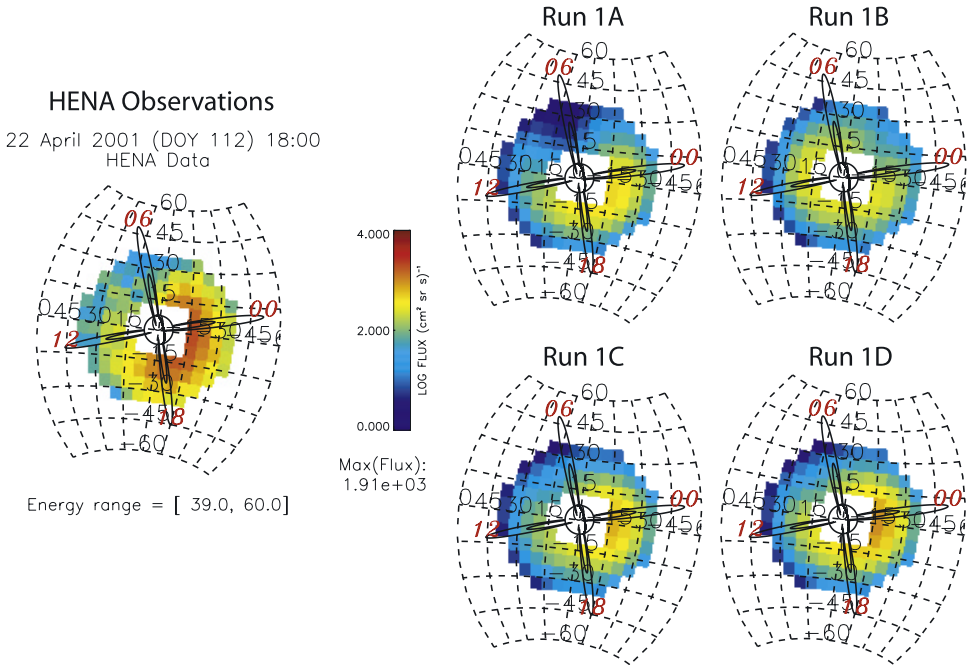

Figure 6. HENA-RAM comparisons of 39–60 keV hydrogen fluxes at 1800 UT on 22 April 2001. The observed image is on the left, and the simulated ENA images, forward modeled from the hot ion results from RAM for each run, are shown on the right. The view is from over the North Pole, with noon to the left and dawn to the top in each image. The fluxes are shown on a logarithmic color scale in units of $(cm^2\ sr\ s)^{-1}$. The black thin lines emanating from Earth in each image are dipole field lines at L = 4 and 8. The dashed grid lines are reference grids in HENA angular space, and each grid step is roughly 2 R_E close to the Earth.

perturbation of *Dst**) with the total ion energy content in the Earth's magnetic field. The derivation of (4) is for an arbitrarily distributed plasma, and it only takes into consideration the cross-magnetic-field currents in the magnetosphere (see the discussion by *Carovillano and Siscoe* [1973]). Application of (4) to RAM results yields a nonphysical westward current at the last grid cell because (4) assumes that all of the plasma pressure is contained in the integration domain (that is, the pressure beyond the outer boundary is assumed to be zero) [*Liemohn*, 2003]. This "truncation current" causes (4) to overestimate the perturbation from the near-Earth plasma. However, this current can be considered as a very crude proxy for the tail current contribution to *Dst**, and therefore its influence has not been removed from the simulated *Dst** values used in these comparisons. Several comparisons are made between *Dst** and Dst^*_{DPS}. The first is with the magnitude of the minimum perturbation value (i.e., the peak intensity of the storm). The second is with the universal time of the *Dst** minimum (the timing of the storm peak). The third and fourth comparisons are between the entire time series, comparing the average perturbation values and the RMS (root mean square) error of this ratio compared against unity (i.e., perfect matching). Note that this average is taken over a 2-day window surrounding the storm peak, including several hours of prestorm time, the entire main phase, and most of the recovery phase of the storm.

[31] The second selected data set is energetic neutral atom (ENA) snapshots from the medium energy neutral atom (MENA) instrument on board the IMAGE spacecraft [*Pollock et al.*, 2000]. ENAs are produced when the hot ions of the ring current charge exchange with the relatively cold neutral hydrogen geocorona (or the upper atmosphere). The resulting hot neutrals are no longer confined by the magnetic field and therefore quickly fly away and are lost from the system. MENA detects these ENAs in the energy range of 1 keV to 60 keV and have revealed the dynamics of the plasma sheet and low-energy ring current during storms and substorms [e.g., *Pollock et al.*, 2001, 2003]. The postprocessing algorithm of *Henderson et al.* [2005] allows for the selection of a single energy (rather than a range) for image production. Two energies are selected for this study, 6 keV and 24 keV. In particular, model results are compared against 10-min integrations beginning at 1800 UT, when the IMAGE satellite was at its closest position to being directly over the North Pole. Choosing this time minimizes line-of-sight variations that can bias the resulting image. Simulated MENA images are produced for each of the simulations for direct comparison against the MENA observations. Individual comparisons are made against the MLT location of the maximum and minimum ENA flux in the *L*-shell range from 2 to 5 (the main ring current region).

[32] The third selected data set is from the high energy neutral atom (HENA) instrument on IMAGE [*Mitchell et al.*, 2000]. This instrument observed ENAs in the 10–200 keV energy range, and its design is less sensitive to background radiation contamination in the signal. HENA observes the peak energies of the storm-time ring current

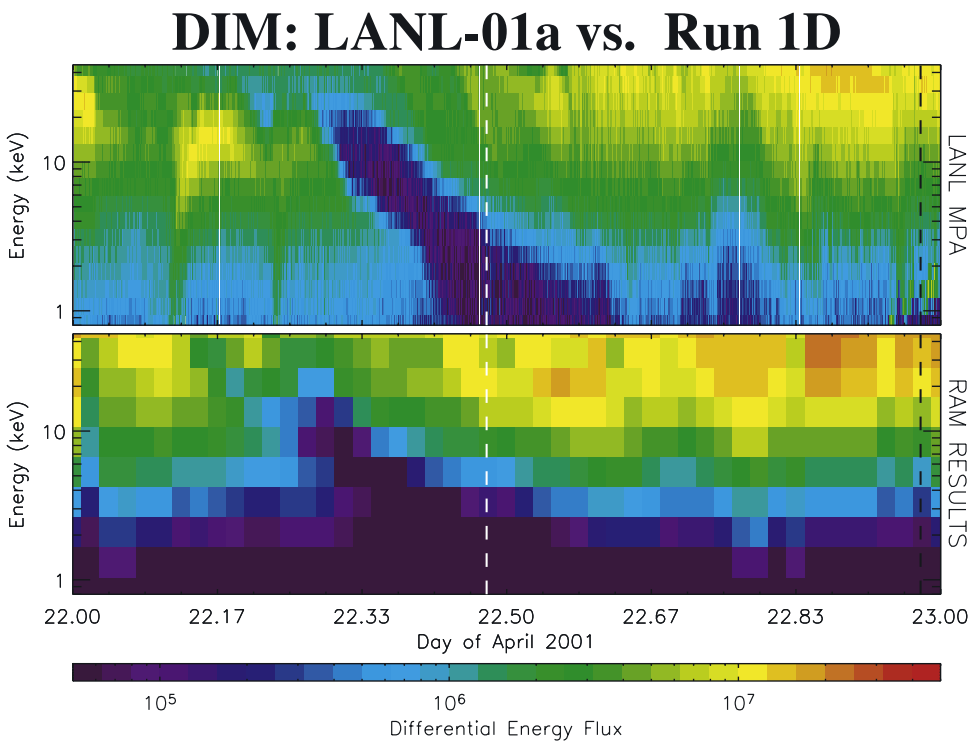

Figure 7. Hot ion differential energy flux comparisons between LANL-01a (upper panel) and RAM results from Run 1D (lower panel). The white and black vertical dashed lines mark local noon and midnight, respectively. The deep ion minimum (DIM) is clearly visible as the region of very low fluxes slanting from noon in the low-energy channels toward earlier times (both local and universal) in the higher-energy channels.

[e.g., *Mitchell et al.*, 2001, 2003; *Brandt et al.*, 2002c, 2002d, 2005]. Three proton energy channels are selected for this comparison: 16–27 keV, 39–60 keV, and 60–119 keV. Again, the start time of the 10-min integration is 1800 UT, when IMAGE was passing almost directly over the North Pole. As above, simulated HENA images were made from the model results and compared against the observations in the L = 2–5.5 radial distance range. Three separate numbers are compared for each energy channel. The first is the local time of the peak in the flux. The second is a ratio of the modeled flux values, summed over the ring of local times in the *L*-shell range of interest, to a similar summation of the observed fluxes in this region. The final comparison is with the RMS error (from each location in the region) of this ratio against unity.

[33] The fourth selected data set is the deep ion minimum (DIM) as observed in the LANL MPA flux spectrograms. This feature results from the energy-dependent drift paths of hot ions through the inner magnetosphere. Low-energy ions tend to drift eastward around dawn and high-energy ions magnetically drift westward around dusk. Depending on the strength and morphology of the convection electric field, this drift separation creates a location-and-energy dependent void in the dayside geosynchronous ion fluxes because the flow paths for some energies stagnate, allowing the fluxes to be attenuated by loss. The DIM widens during low convection intervals and narrows during times of high convection. Note that *Thomsen* [2004] also showed that nightside MPA electron flux measurements are excellent delineators of magnetospheric convection. Therefore during a storm main phase, this feature should be a good indicator of the validity of the selected electric field models in the simulations. For each storm, DIM observations from three LANL satellites are included: for storm 1, they are 1991-080 (local noon at 2300 UT), 1994-084 (local noon at 0500 UT), and LANL-01a (local noon at 1130 UT); and for storm 2, they are 1994-084 (local noon at 0500 UT), LANL-97a (local noon at 0720 UT), and LANL-01a (local noon at 1130 UT). All three DIM observations are taken during the main phase of each storm. Two comparisons are included, both relating to the DIM signature in the 4 keV flux channel (an energy that consistently shows a clear DIM). The first is the UT of the DIM, which is directly related to the MLT because the satellites are in geosynchronous orbit. The second is the minimum value of the hot ion flux at this location. Note that the RAM fluxes include both H^+ and O^+ for proper comparison against the total ion flux observed by MPA.

[34] The fifth selected data set is dayside moments (density and temperature) as measured by MPA on the LANL spacecraft [*Thomsen et al.*, 1999]. The same three LANL satellites are used for this comparison as were chosen for the flux comparisons, and the moments are taken only from the MPA instrument (that is, for plasma energies up to 40 keV). MPA moments have been shown to systematically vary with local time and geomagnetic activity [*Korth et al.*, 1999; *Denton et al.*, 2005a]. The time selected for this comparison is local noon. Because the LANL data set is used as the nightside boundary condition for the RAM simulations, comparing at noon (and only there) is thought to be an appropriate check of the simulated transport and

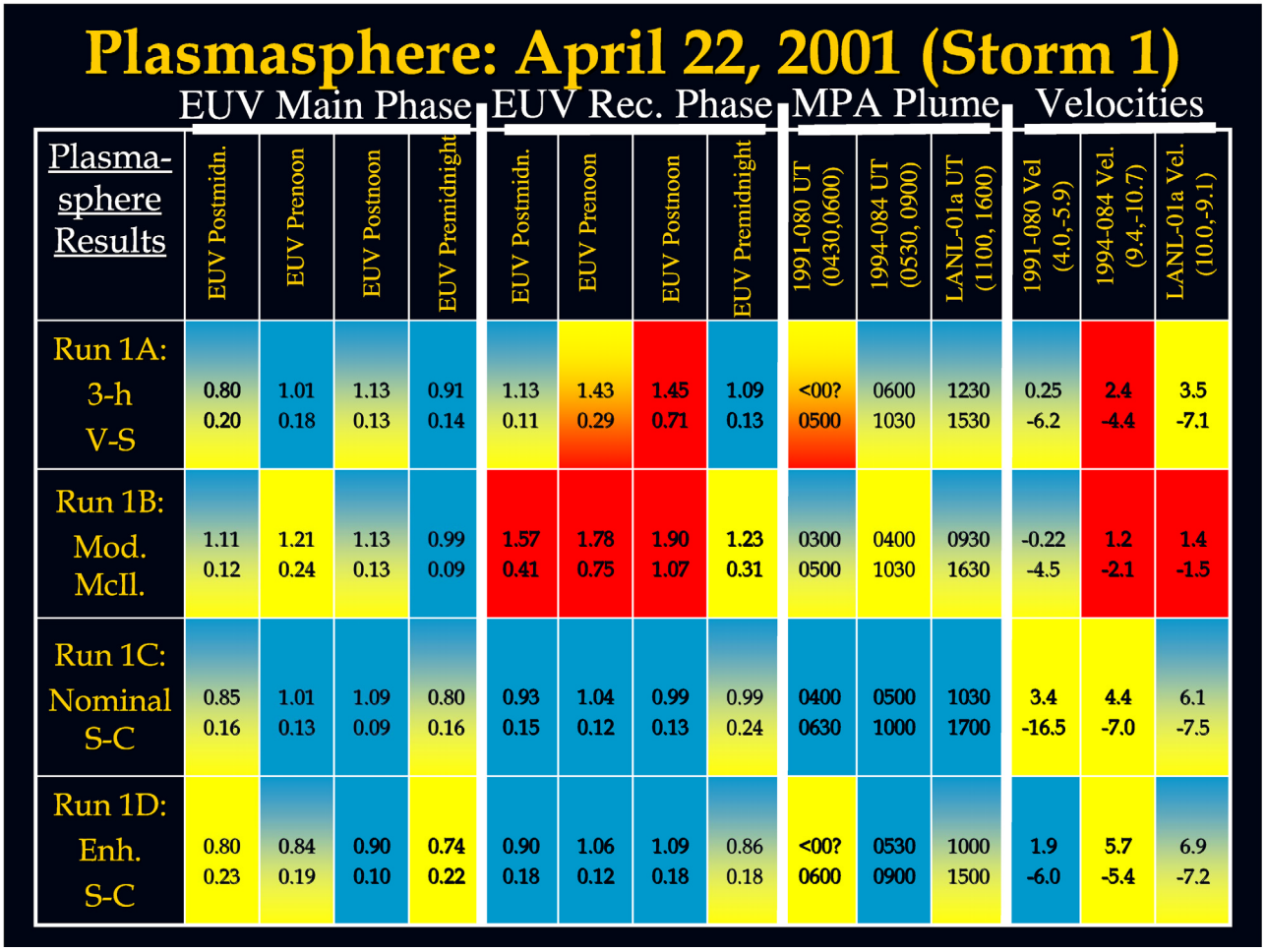

Figure 8. Quantitative assessments of plasmasphere data-model comparisons for the April 2001 storm. The four rows give the results for the four simulations for this storm, while each of the 13 columns are for a different data set (in order: EUV main phase orbit, EUV recovery phase orbit, MPA plume, and MPA plume-averaged drift velocities). Color assignments for each block are made according to the accuracy levels specified in Table 1. Numbers in the column headers are data-derived quantities, for comparison with the values in the column boxes.

loss through the inner magnetosphere. Two moments are considered, the density and the perpendicular temperature. The MPA density is compared against the weighted sum density from the RAM simulations, $n_{total} = n_{H^+} + 0.25n_{O^+}$, to account for the fact that MPA does not resolve the ion composition. The MPA $T_\perp$ value is compared against the modeled O^+ $T_\perp$ value because the H^+ boundary condition includes SOPA fluxes which inflate the high-energy tail of that species. The nightside O^+ boundary condition is purely from the MPA observations and is therefore a more suitable number for dayside comparison.

[35] The sixth data set used for comparison is the plasmapause as extracted from snapshots of the IMAGE extreme ultraviolet (EUV) instrument [*Sandel et al.*, 2000]. This detector measures 30.4 nm photons from the near-Earth region. In particular, it observes solar photons that have been scattered from the helium ions in the Earth's ionosphere and plasmasphere. The line of sight integrals often reveal a well-defined plasmasphere, showing distinct features in its outer boundary (the plasmapause) such as plumes, shoulders, fingers, and notches [e.g., *Sandel et al.*, 2001, 2003]. The images can be mapped to an equatorial plane view of the data, allowing for direct comparison with magnetospheric processes. Manual extractions of the steep density drop (the plasmapause) can be performed for each 10-min integration from the instrument, yielding a time series progression of the outer boundary of the plasmasphere throughout a storm event (at least while IMAGE is near apogee). This was done for the two selected storms and the results are summarized by *Goldstein et al.* [2005]. Because the cold particles of the plasmasphere are not subjected to the complicating factor of magnetic drifts, the dynamics of the plasmapause is an excellent measure of the convective electric field [e.g., *Goldstein et al.*, 2004].

[36] These comparisons are divided into two groups, the first during the main phase of the storm and the second during the storm peak and recovery phase (for each storm). Gradients of log(density) from the DGCPM simulation results were calculated and the maximum gradient was compared against the plasmapause locations extracted from the EUV images. These comparisons were done every 30 min during two consecutive IMAGE apogee passes

Table 1. Description of the Quantitative Data-Model Comparisons

Name	Blue	Blue/Yellow	Yellow	Yellow/Red	Red
Dst* minimum, nT	≤20	(20, 30]	(30, 40]	(40, 50]	>50
Dst* minimum UT, hours	≤1	(1, 2]	(2, 3]	(3, 4]	>4
Dst* ratio − 1	<0.1	(0.1, 0.2]	(0.2, 0.3]	(0.3, 0.4]	>0.4
Dst* ratio RMS	<0.1	(0.1, 0.2]	(0.2, 0.3]	(0.3, 0.4]	>0.4
MENA extrema MLT, hours	<2	3–4	5–6	7–8	≥9
HENA flux ratio	[1, 1.5]	(1.5, 2]	(2, 3]	(3, 5]	>5
HENA ratio RMS	≤0.5	(0.5, 0.75]	(0.75, 1]	(1, 2]	>2
HENA peak MLT, hours	≤1	2	3–4	5	≥6
LANL DIM UT, hours	≤0.5	1	1.5–2	2.5	≥3
LANL DIM flux ratio	≤2	(2, 4]	(4, 7]	(7, 10]	>10
LANL density, cm^{-3}	≤0.1	0.2–0.3	0.4–0.5	0.6–0.7	≥0.8
LANL temperature, keV	≤1	2	3	4	≥5
EUV plasmapause ratio	[1, 1.1]	(1.1, 1.2]	(1.2, 1.3]	(1.3, 1.4]	>1.4
EUV plasmapause RMS	≤0.1	(0.1, 0.2]	(0.2, 0.3]	(0.3, 0.4]	>0.4
LANL plume MLT, hours	≤0.5	1	1.5–2	2.5	≥3
LANL velocity, km/s	≤2	(2, 3]	(3, 5]	(5, 6]	>6

(the two groups), yielding nearly 20 comparisons for each storm phase. Each individual UT comparison is further divided according to MLT quadrant (postmidnight: 0000–0600, prenoon: 0600–1200, postnoon: 1200–1800, and premidnight: 1800–2400). This division is made because the dynamics of the plasmapause are quite different between the quadrants, and this breakdown of the results has been shown to highlight differences between electric field models [*Liemohn et al.*, 2004, 2005]. Two separate numbers are evaluated. The first is the average model-to-data ratio of the plasmapause *L*-shell at a given local time, averaged over the number of data points in the quadrant for the ten snapshots during an apogee pass. The second is the RMS error of this ratio compared against unity.

[37] The seventh data set is the location of the observed plasmaspheric drainage plume from the LANL MPA instruments. The same three geosynchronous LANL satellites are used (for each storm) as were chosen for the ring current comparisons. These three provide observations of the dayside drainage plume at various MLTs and UTs throughout the main phase of the storm. The plasmasphere has a clear signature on the MPA spectrograms in the 0–100 eV ion energy channels, and it is relatively easy to identify the times of plume observation. Such observations have been extensively used to understand magnetospheric convection [e.g., *Weiss et al.*, 1997; *Elphic et al.*, 1997; *Ober et al.*, 1997a; *Su et al.*, 2001]. To quantify and automate this identification process, however, a density threshold of 3 cm^{-3} (for this ion energy range) is used as the demarcation of a plasmaspheric observation. Two values are compared, the start and end universal times of plume observation for each satellite.

[38] The eighth and final data set is the equatorial plane velocity within the plasmaspheric drainage plume, as seen by the LANL MPA instruments. This is the just about the only time when the MPA instrument can obtain reliable measurements of the drift velocity (that is, when the cold ion density is large) [*Thomsen et al.*, 1999]. Two numbers are compared, the radial and the azimuthal drift speeds. The observations are quite noisy, and so it is prudent and useful to instead compare against the speeds after averaging across the plume width. Therefore this averaging was done for both the data and the model results. Because the data are averaged over the length of the drainage plume observations, the time coverage of these comparisons spans much of the main phase of the storm. The typical local time of the comparisons is the early afternoon sector (specifically, the MLT of the plasmaspheric drainage plume during the main phase, as seen by each satellite).

[39] The data-model comparison philosophy of this study is to perform quantitative assessment of the similarity of the simulation results with the observations, both for individual data sets and for the entire collection as a whole. Therefore to compare the accuracy with one data set against the accuracy with another, completely different type of data set, a common scaling system has been developed to normalize the comparison, with five gradations for the goodness-of-fit. Table 1 lists the data-model comparisons conducted for this study as well as the cutoff values for assigning a color to a specific value. Once colors have been assigned to each of the individual comparisons, a numeric value of 1 (blue) through 5 (red) is used to quantitatively assess the accuracy of the simulation, integrated across the data sets.

[40] While most of the data-model comparison values listed in Table 1 are self-explanatory, a few require additional notes. RMS is short for root-mean-square and has the standard definition for this quantity. DIM is short for deep ion minimum, which is a regular dayside feature of the LANL MPA flux spectrograms resulting from the stagnation of drift through the inner magnetosphere for certain ion energy-per-charge ratios. Note that the two "flux ratio" comparisons actually can have values either above or below unity, but only the gradation cutoffs above unity are listed in Table 1. That is, there is a second set of ranges for ratios below unity (that is, divide one by all of the numbers in those rows to get the second half of the color assignment ranges). Likewise, the *Dst** ratio comparison can be either positive or negative, yet only the positive ranges are listed in Table 1. So, again, there is a second set of color assignment ranges with negative values to those listed.

[41] In the assessment summary charts below, each box on the chart contains several (usually two or three) individual data-model comparisons. When assigning a numeric value (1 through 5, blue-yellow-red) to a particular box, the

numeric values for each of the comparisons is arithmetically averaged, and a single value/color is assigned for that box.

4. Results for the April 2001 Storm

[42] The data-model comparisons described above were conducted for storm 1. The sections below detail the assessments of the ring current and plasmasphere results from the runs with the four electric field descriptions.

4.1. Ring Current Data-Model Comparisons for April 2001

[43] Figure 5 presents the summary results for the ring current data-model comparisons for storm 1. The 13 columns each represent a different data set, and in most cases each column contains several data-model comparisons. The first column of Figure 5 compares the magnitude and timing of the storm peak, as measured by *Dst** and modeled by Dst^*_{DPS}. In the header for this column, the two numbers listed in parentheses are the observed *Dst** minimum (−90.8 nT) and its UT on 22 April (1500 UT). In each box below this are the corresponding modeled values for each of the four simulations. The second column of Figure 5 presents comparisons between the time series averages of the observed and modeled *Dst** values. In each box, two numbers are listed, the model-to-data ratios, minus one (so zero indicates the same average magnetic depression) and the RMS error between these two time series.

[44] It is seen that three of the field descriptions (B, C, and D) performed essentially equally well in their comparisons with this data set, while field A was slightly less good in matching *Dst**. In the supplemental figure storm1_Dst.eps, it is seen that run 1A did not produce a distinct peak around 1500 UT on 22 April but rather peaked 5 hours later. During the recovery phase, however, this run was as close as any other to the observed time series. None of the simulations, however, produced the secondary storm peak on 23 April. From Figure 1, it is seen that while there was a mild convection increase during this interval (Figures 1f and 1g), there was not a particularly large plasma density enhancement (Figure 1d) to cause an additional ring current intensification.

[45] The next two columns of Figure 5 show comparisons with MENA observations at 1800 UT of 6 and 24 keV atoms, respectively. The two numbers listed in parentheses in the header of each column are the MLT values of the observed maximum and minimum, respectively. The numbers in each box are the corresponding MLTs of the simulated maximum and minimum. The absolute values of the two MLT differences are added together and compared against the values listed in Table 1 to assign a color to each box in these two columns.

[46] It is seen that most of the comparisons with the MENA peak locations are very good, with each of the simulated extrema within 2 MLT hours of the observed location. The only one that seems to be significantly different is run 1B's comparison at 24 keV. Both of the simulated extrema are shifted westward from where they were observed. The westward shift is perhaps surprising because the modified McIlwain field produces a strong eastward flow across the morningside. The difference is in the dayside convection strength, which is much weaker in this field than in the others (see Figures 3 and 4). Therefore the flux minimum during the main phase is shifted toward dawn (i.e., westward) relative to the minimum produced by the other fields. The UT of this comparison is just past the peak of the storm, and therefore the convection is reduced and the 24 keV protons are flowing westward due to the dominant magnetic drift term (in all of the field models). Because the fluxes are starting from a relatively westward location, they are still shifted at this UT. This is not the case for the 6 keV protons, for which corotation and magnetic drifts are comparable at typical ring current altitudes.

[47] The next three columns in Figure 5 present the comparisons with HENA snapshots at 1800 UT (energy channels of 16–27 keV, 39–60 keV, and 60–119 keV, respectively). The parenthetical number in the header of each column gives the MLT value of the observed flux peak. In each box in these columns, three numbers are listed: the MLT value of the simulated ENA flux peak, the average of the model-to-data flux ratio from each pixel in the 2 to 5.5 L shell range, and the RMS error of this ratio against unity.

[48] The comparisons are not as good as with the MENA data. This is expected, though, because this comparison includes quantitative flux ratios as well as the location of the peak. It is seen that all of the comparisons reveal a modeled average ring current flux that is less than that observed (for all four runs at all three energies). The underprediction ranges from a factor of 2 to a factor of 7. Most of the simulations, however, correctly predicted the location of the peak (again, within 2 hours of the observed location). Only two of the comparisons are beyond this difference, the two higher-energy channels of run 1B. Again, the peaks are shifted westward, revealing a systemic problem of the modified McIlwain field description for recovery-phase high-energy ion fluxes.

[49] Figure 6 shows the observed and simulated (forward modeled) energetic neutral atom flux images for the first column of the HENA-RAM comparisons (i.e., for 39–60 keV energy). The view is over the North Pole, with the Sun to the left and dawn to the top in each image. The grid is in HENA angle space and each grid step roughly corresponds to 2 R_E close to the Earth. The underestimation of the measured ENA fluxes is clearly seen in this figure. The simulated spatial distribution of the fluxes, however, is similar to that observed by HENA. For instance, the self-consistent field models (runs 1C and 1D) predict a flux peak just duskward of midnight and a flux minimum just sunward of dawn. These are the same local times for these extrema as seen in the data. In run 1A, the flux minimum is shifted to slightly earlier local times, and this westward shift is even larger in run 1B.

[50] Columns 8–10 of Figure 5 show comparisons against main phase DIM observations in the 4 keV energy channel by MPA on three different LANL spacecraft (satellites 1991-080, 1994-084, and LANL-01a, respectively). The two numbers in each column header are the observed UT and the minimum flux value. In each box in the columns, the simulated UT and minimum flux value for this energy is listed.

[51] The data-model comparisons for the deep ion minimum are very good for all of the runs and for all of the satellites. While some of the modeled DIMs are much

clearer than others in the energy-time spectrograms, they all produced a DIM at roughly the right time with roughly the right depth (for the selected energy channel). Figure 7 shows an exceptionally good comparison, in which the observed location and depth of the DIM is closely matched by one of the simulations (run 1D). The energy-time spectrograms span the 24 hours of 22 April and the entire "hot ion" energy range of MPA (100 eV to ~45 keV). The black and white lines demark local midnight and noon, respectively.

[52] The similarity in goodness of comparison of the four runs is perhaps surprising because of the differences in the dayside convection strengths (particularly field B). It is actually expected, though, because the analytical models were originally created to match geosynchronous observations. In addition, the convection during this interval is not particularly intense (compared to the main phase of storm 2), and therefore the analytical field descriptions, which in general are valid for low to moderate convection levels, are still appropriate and yield a good comparison with the LANL MPA fluxes.

[53] The final three columns of Figure 5 present data-model comparisons of hot ion density and temperature at local noon (for the same satellites: 1991-080, 1994-084, and LANL-01a, respectively). The two numbers listed in the column headers are the observed density and temperature, respectively. Listed in each box in the columns are the simulated values at the same local time and universal time as the satellite to which it is being compared.

[54] As with the LANL flux comparisons, the LANL moments comparisons against the model results are also very good. The modeled moment values are all quite close to the observed values. The exception to this comment are the comparisons with the 1994-084 densities, which are all a factor of two or more larger than the measurement density. It appears that the dayside LANL observations are not a particularly good discriminator between the electric field descriptions because the simulation results are all so similar.

4.2. Plasmasphere Data-Model Comparisons for April 2001

[55] Figure 8 presents a summary of the plasmaspheric data-model comparisons for storm 1. As in Figure 5, each of the 14 columns represents an assessment against a different data set, with several specific values being compared for each one.

[56] The first eight columns of Figure 8 are all comparisons against plasmapause observations from IMAGE-EUV. The first group of four columns shows comparisons during the main phase of the storm (2300 UT on 21 April to 0800 UT on 22 April) and the second group presents comparisons during the storm peak and recovery phase (1330 UT to 2230 UT on 22 April). The columns within each group give the results for each local time quadrant (postmidnight: 0000–0600, prenoon: 0600–1200, postnoon: 1200–1800, and premidnight: 1800–2400). Two numbers listed in each box are as follows: the average model-to-data ratio of the plasmapause L-shell at a given local time (averaged over the apogee pass), and the RMS error of this ratio compared against unity.

[57] First, consider the main phase results (the first four columns of Figure 8). They all seem to be decently good, with the observed and modeled plasmapause L shells usually within 10% of each other, with relatively low spread. Only a few of the comparisons in these columns are more than 20% off. Specifically, the prenoon sector plasmapause from run 1B is, on average 21% farther out than that observed. This is because of the weak electric field across the dayside in this field description. Another subpar comparison is the nightside plasmapause from run 1D, which is on average more than 20% inward from the observed location. This is because the enhanced conductance reduces the shield potential from the storm-time region 2 FACs, and the large-scale convection penetrates more easily into the inner magnetosphere than it does for other field descriptions (specifically, compare with the nightside results for run 1C). It is clear from this result that the convection was unrealistically undershielded in run 1D.

[58] Now consider the recovery phase results (columns 5–8 of Figure 8). The plasmapause is already compressed, the shrunken plasmasphere is starting to corotate again, and the drainage plume is beginning to wrap around the plasmasphere. The results for runs 1C and 1D are better than in the main phase, with predicted plasmapause locations very close to those observed (usually well within 10%). The results from runs 1A and 1B, however, are not as good as they were in the main phase, with the simulated location farther out than the observed plasmapause. This is especially true for the dayside, where the errors are quite large, but the nightside is also systematically different from the observation location. It appears that the plasmasphere continued to collapse between the two IMAGE apogees while the analytical electric field models did not predict this inward motion.

[59] This is illustrated in Figure 9, in which some of the recovery phase plasmapause comparisons between EUV and run 1A are presented. The plasmapause locations extracted from the EUV images are shown as white circles, while the color scale shows the magnitude of the thermal plasma gradient as calculated by DGCPM. These comparisons are shown because they demonstrate the range of goodness of fit. The simulated plasmapause is clearly visible as a bright and narrow band of large gradients, surrounded by small and slowly varying gradient values. On the nightside, the simulation results follow the shape of the observed values but are slightly farther out than the observed location. On the dayside, however, the modeled plasmasphere is substantially larger than that seen in the EUV images. This is because field B did not replicate some enhanced electric field on the dawnside of the inner magnetosphere.

[60] The next three columns of Figure 8 present comparisons of the location of the modeled plasmaspheric drainage plume with observations from the LANL MPA instruments. The three columns are comparisons with different geosynchronous LANL satellites: 1990-080, 1994-084, and LANL-01a, respectively. The two numbers listed in parentheses in the column headers give the UT values of the start and end times of plume observation for that satellite. These are to be compared against the two numbers in each box within the column, which list the modeled start and end universal times, based on the satellite's location in the simulation domain.

[61] Most of the plume comparisons are quite good. Run 1C, for instance, predicted all eight times within an

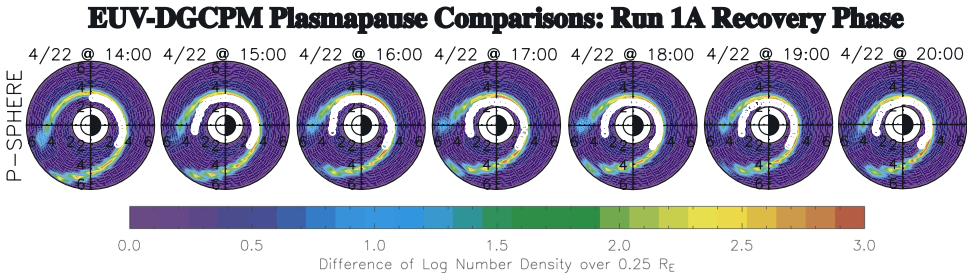

Figure 9. Comparisons between the plasmapause locations extracted from EUV images and the plasmaspheric density gradients in the DGCPM results for run 1A. The seven plots show a time progression (every hour) during the recovery phase of storm 1. The view is over the North Pole with the Sun to the left and dawn to the top in each plot, and distances are marked in R_E. The white circles denote the EUV-derived plasmapause locations, while the color scale shows the logarithm of the absolute value of the simulated thermal plasma density gradient.

hour of when they were observed. All of the other simulations produced at least a few times very close to the MPA value. However, there are some notable exceptions, particularly the start times for runs 1A and 1D for the 1990-080 comparisons. In the auxiliary files, it is seen that these plumes begin somewhere off the plot (that is, on 21 April), many hours before the observations actually began. These simulations have plumes reaching geosynchronous orbit near local noon late on 21 April, whereas in the other two simulations, the plume does not reach geosynchronous orbit until early on 22 April. This is because of the enhanced convection early in the simulation. In run 1A, this is from the *Kp* index rising ahead of the SSC because of its 3-hour averaging. In run 1D, this is because of the enhanced conductance reducing the shielding potential and allowing the large-scale convection to strip away the plasmasphere faster than with the nominal conductance setting (run 1C).

[62] The final three columns of Figure 8 show comparisons of the equatorial plane velocities within the MPA-observed plasmaspheric drainage plume. The two numbers in the column headings give the average radial (positive outward) and azimuthal (positive westward) flow velocities, in km/s, from the MPA measurements. The simulated radial and azimuthal speed, averaged over the same MLT-UT interval, is given in each box in these columns.

[63] It is seen that the self-consistent electric fields are systematically better at matching the measured velocities than the analytical electric fields for this storm main phase. In general, the modeled average values are lower in magnitude than the observations (only three of the 24 comparisons have the modeled value larger than the data value). However, the direction of the flow is nearly always correct (radially outward and azimuthally westward). The observations exhibit large oscillations and variability, with up to ±10 km/s swings in the data about the mean. This structure is not reproduced by any of the modeled electric fields, and it most likely plasma or MHD wave turbulence not included in the field descriptions.

5. Results for the October 2001 Storm

[64] As was just presented in section 4 for storm 1, data-model comparisons were also conducted for storm 2. The sections below detail the assessments of the ring current and plasmasphere results from the runs with the four electric field descriptions.

5.1. Ring Current Data-Model Comparisons for October 2001

[65] A summary of the ring current data-model comparisons for storm 2 is given in Figure 10. The first two columns of Figure 10 present *Dst** comparisons with its simulation-based analogue, Dst^*_{DPS}. The various numbers in these columns are the same as in Figure 5. The header numbers in the first column give the observed *Dst** minimum (−170.9 nT) and the time it occurred on 21 October (2100 UT). The values in the column boxes are the corresponding simulated Dst^*_{DPS} minimum and its timing from each simulation. In the second column, the numbers in the boxes give the model-to-data ratio (minus one) over a 2-day window surrounding the peak and the RMS error of this ratio.

[66] The *Dst** comparisons reveal an interesting result: the analytical field models outperformed the self-consistent field models in matching this data set. All of the runs reproduced the timing of the first *Dst** minimum, so this is not the reason. The real difference is seen in model-to-data ratio averages, in which the analytical models are both within 20% of the observed values while the self-consistent results are not. That is, over the course of the 2-day interval contributing to this comparison, the self-consistent fields produced a consistently weaker ring current than did the analytical fields.

[67] The auxiliary files illuminate the reason for this unexpected result. It is seen that the self-consistent runs match the initial main phase quite well, reproducing the timing and depth of the first *Dst* minimum. After this phase, however, the self-consistent runs diverge from the observed *Dst** values. They recover more rapidly than observed during the first half of 22 October and then do not reintensify to match the second *Dst** minimum. The trends in the modeled *Dst** time series appear to be correct, matching the slope of the observed *Dst** values during the second storm peak, but the magnitude is off by about 40 nT. Contrast this with the *Dst** from run 2A (the Volland-Stern field). It also reproduced the first *Dst** minimum and then overrecovered early on 22 October. It hit the second *Dst** minimum, however, because its intensification was larger

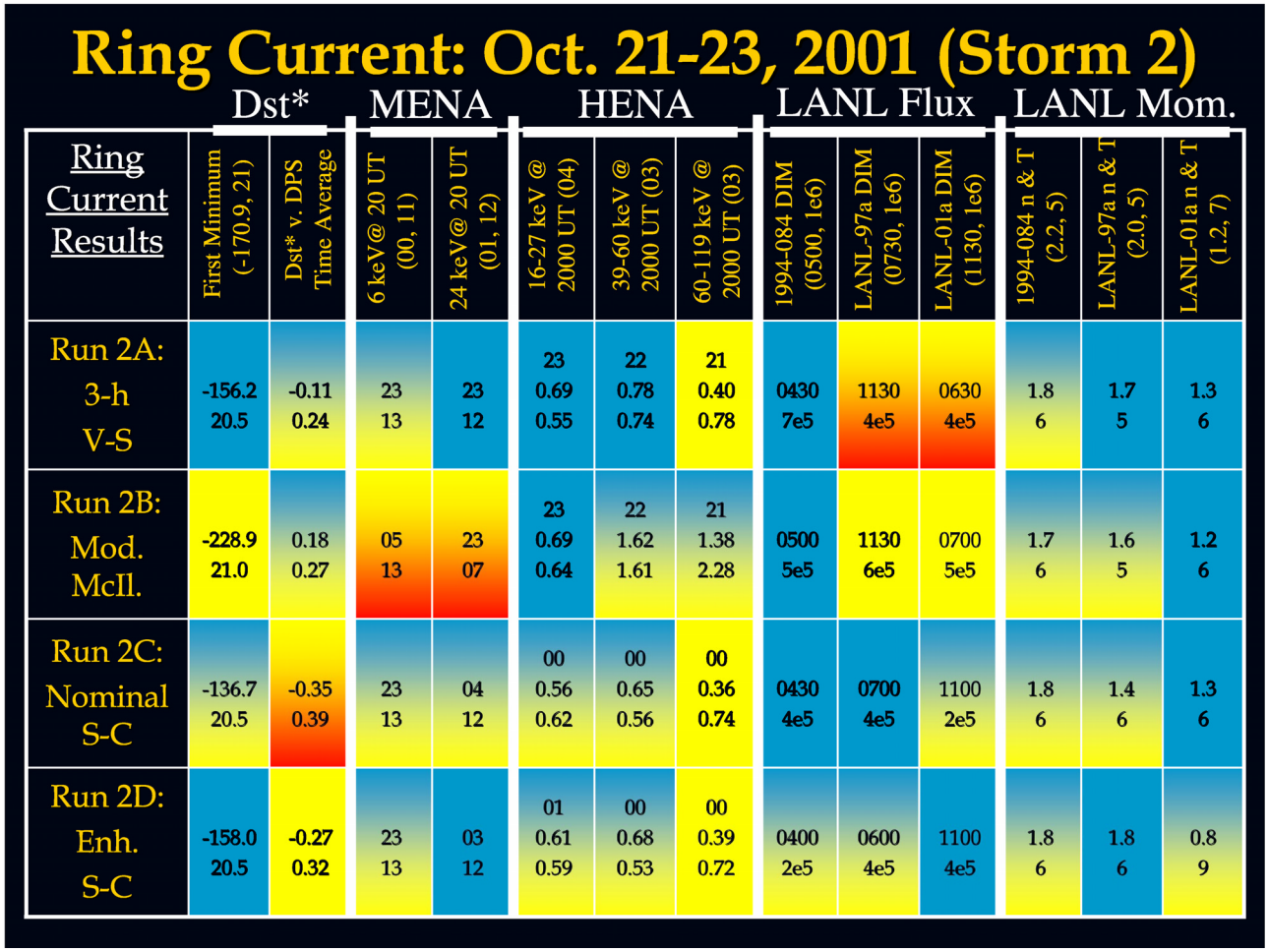

Figure 10. Quantitative assessments of ring current data-model comparisons for the October 2001 storm. The format is the same as that in Figure 5.

than that produced by the self-consistent fields. The *Dst** from run 2B (modified McIlwain field) overpredicted the depth of the first *Dst** minimum by over 60 nT. After this, though, it also overrecovered early on 22 October and then closely followed the observed *Dst** time series through the second storm peak. The net result is that the analytical fields kept their modeled *Dst** value closer to the observed values for more of the storm interval than did the self-consistent fields. The self-consistent fields, however, matched the trends (i.e., slopes) of *Dst** better than the analytical fields, except for the intrapeak lull in activity.

[68] The third and fourth columns of Figure 10 present model comparisons with MENA observations at 6 and 24 keV energy at 2000 UT on 21 October. The numbers in the column headers are the MLT values of the flux maximum and minimum, respectively, extracted from the MENA images, and the numbers in each box are the corresponding MLT values of the ENA flux maximum and minimum taken from the forward modeled simulation results.

[69] The comparisons against the peak flux MLTs from the MENA images show that three of the four fields matched the data quite well. Run 2B, however, missed both the 6 keV and the 24 keV peak locations, to the east and the west, respectively. The time of these comparisons is late in the first main phase of the storm sequence. Therefore the strong dawnside electric fields in the modified McIlwain field are still present, causing the low-energy ions to excessively drift eastward and thus the peak location was poorly reproduced. The other field models produced ENA peaks that were all quite close to the observed peaks.

[70] The next three columns in Figure 10 show the HENA-RAM comparisons at 2000 UT. The numbers in the column headers give the MLT of the observed flux peak. The three numbers in each box are as follows: the simulated ENA flux peak; the model-to-data ratio of the fluxes, averaged over all lines of sight passing through 2 and 5.5 R_E equatorial plane distance; and the RMS error of this ratio compared against unity.

[71] The HENA comparisons for storm 2 are, in general, better than those for storm 1. The analytical models slightly outperformed the self-consistent models, but not by much. The self-consistent fields matched the location of the flux peak better than the analytical models, but the analytical models did better at reproducing the average flux level in the L = 2–5.5 range.

[72] Columns 8–10 of Figure 10 present model comparison with the DIM observations from the LANL MPA

instruments. The three LANL satellites chosen for this comparison are 1994-084 (local noon at 0500 UT), LANL-97a (local noon at 0720 UT), and LANL-01a (local noon at 1130 UT). Therefore all of these DIM comparisons are taken from 22 October, during the hiatus in southward IMF during the first half of the magnetic cloud passage. The numbers in the column headers are the UT of the DIM as seen in the 4 keV ion energy channel and the differential number flux value at this time. The numbers in each box are the corresponding simulation results for the DIM, as extracted from the results along each satellite trajectory.

[73] The LANL flux comparisons of the deep ion minimum location and depth reveal a different trend: the self-consistent models were more accurate than the analytical models. The three LANL satellites chosen for this comparison are 1994-084 (local noon at 0500 UT), LANL-97a (local noon at 0720 UT), and LANL-01a (local noon at 1130 UT). Therefore all of these DIM comparisons are taken from 22 October, during the hiatus in southward IMF during the first half of the magnetic cloud passage. It is seen that the analytical models badly miss the observed location of the DIM for two of the three comparisons (the later two), being 4 hours late in for LANL-97a and 4–5 hours early for LANL-01a. The DIM is shifting in local time in these simulations while it is not greatly shifting in local time in the observations or in the self-consistent results (where it is close to local noon for this energy channel).

[74] The final ring current comparisons are with the LANL moments at local noon for these same three satellites. The two numbers in each column header give the observed density and perpendicular temperature from the MPA hot ion measurements. The two numbers in each box give the simulated density ($[H^+]$ plus 0.25 times $[O^+]$, for direct comparison against the non-mass-resolved MPA value) and perpendicular temperature (from O^+, again for direct comparison without SOPA flux interference).

[75] These data-model comparisons are quite good for all of the simulations. On average, the observed storm 2 densities (temperatures) are higher (lower) compared to the observations from storm 1. This is consistent with statistical analyses of LANL MPA moments, considering the increased strength of storm 2 compared to storm 1 [*Korth et al.*, 1999; *Denton et al.*, 2005a; *Zhang et al.*, 2006]. The simulations, in general, reproduce this trend for both storms.

5.2. Plasmasphere Data-Model Comparisons for October 2001

[76] Plasmaspheric comparisons were also conducted for storm 2, and the summary of this assessment is shown in Figure 11. As with storm 1, two consecutive apogee passes of IMAGE EUV snapshots of the plasmasphere were used to compare an observed plasmapause location with that derived from the simulations. The two orbits yield results in both the first main phase (late on 21 October) and the first recovery phase (during the lull in activity early on 22 October). The columns within each group (group meaning main phase and recovery phase orbit) give the results for each local time quadrant. Two numbers listed in each box are the average model-to-data ratio of the plasmapause *L*-shell (averaged over the apogee pass for each quadrant), and the RMS error of this ratio compared against unity.

[77] The summary chart for the main phase comparisons reveals mixed success for all of the selected field models. In general, they all predict a plasmapause that is farther out than the observed location. Run 2B is noticeably worse than the other three runs, which are all roughly equal in their ability to reproduce the observed plasmapause location.

[78] The recovery phase comparisons are better, though. Runs 2A and 2C are both quite good, especially in the two morning sectors. Run 2D is also fairly good in these two sectors, but underpredicted the plasmapause radial distance in the postnoon sector. Run 2B is still not particularly good across the morning and is clearly the worst of the four field descriptions at reproducing these data.

[79] Columns 9–11 of Figure 11 present data-model comparisons of the plasmaspheric drainage plume location. The three LANL satellites are the same as those used in the ring current comparisons for this storm (1994-084, LANL-97a, and LANL-01a). They all cross local noon during morning UT, and so the plume observations are all from early on 22 October. The numbers in the column headers are the UT values of the start and end times of plume observation in the MPA low-energy ion flux channels. The two numbers in each box in these columns give the plume start and end UT values from the simulation results, as extracted along the satellite trajectories in the computation domain.

[80] The MPA plume comparisons for storm 2 are all quite good. The four runs did well at matching the start and end times of the plume observations, and run 2A did the best. This is interesting because this run was the worst at matching the DIM location observed by these same satellites (see Figure 10).

[81] The final comparison to be presented in this study is between the observed drainage plume velocities (averaged across the plume width) and the modeled plume velocities (also averaged for the same MLT-UT interval). These are shown in the last three columns of Figure 11. The two numbers in parentheses in the column headers give the radial velocity (positive outward) and azimuthal velocity (positive westward), respectively, as computed from the MPA measurements, and the two numbers in each box are the corresponding simulated values.

[82] The runs were all roughly equal in their ability to match the data from each satellite. For 1994-084, all of the comparisons are excellent. For LANL-97a, the comparisons are good. For LANL-01a, the models all did poorly. Again, the models typically underestimate the average flow speeds and also do not reproduce any of the variability of the velocities within the plume. The directions of the mean flow are usually correctly predicted, however. The oscillations are larger for storm 2 than for storm 1, with typical swings of ±20 km/s and some amplitudes reaching ±40 km/s from the mean.

6. Synthesis Analysis

[83] It is a goal of this study to quantify the accuracy of the selected field models at reproducing the observed plasma features of the inner magnetosphere during these storms. With all of the individual data-model comparisons presented in the previous two sections, it is possible to condense these results into aggregate values for each data (for each run) and then further condense the result into a

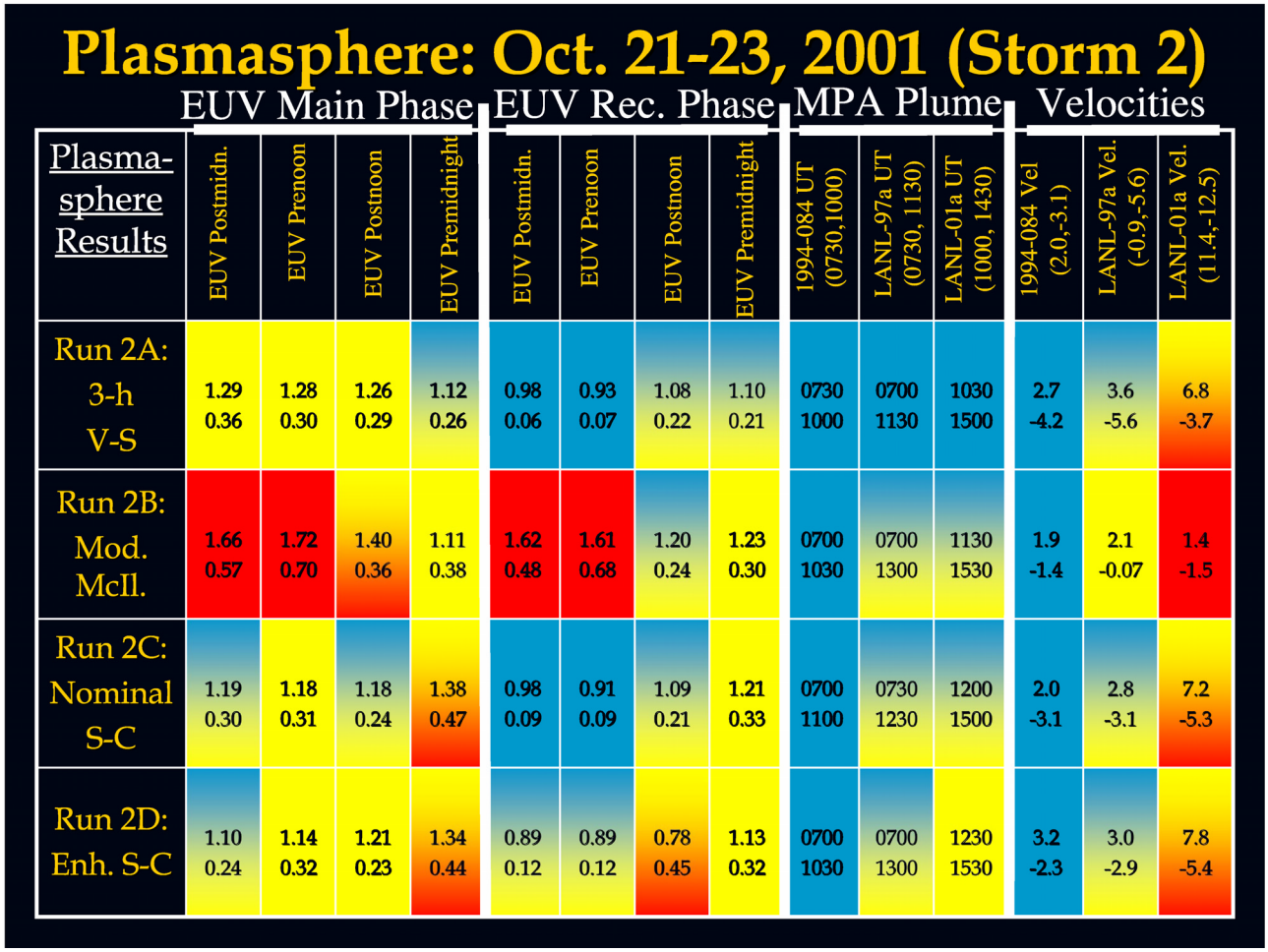

Figure 11. Quantitative assessments of plasmasphere data-model comparisons for the October 2001 storm. The format is the same as that in Figure 8.

single overall assessment for each run, for each storm, and for each field description.

[84] The first step in coalescing these results is to average the assessments within each data type (for each run). First, convert the color assignments in Figures 5, 8, 10, and 11 into numerical values (blue = 1 up to red = 5). Then, sum these values for the columns between each of the heavy white vertical lines in these figures. This yields five ring current categories and four plasmasphere categories. These values are presented graphically in Figures 12 and 13 for storm 1 and storm 2, respectively. In these figures, the resulting averages have again been assigned colors to better illustrate the accuracy of the run results.

[85] The second step in coalescing the results is to average these average values into a single numerical assessment. Table 2 presents these overall assessments, averaged over several groupings. The first grouping is by run, the second grouping is by storm, and the third grouping is by electric field model.

[86] Consider storm 1 first. It is seen in Figure 12 that run 1A is mostly shaded yellow, with some blue in the matrix as well. This indicates that the results were fair at reproducing the data, and it was only good for a few of the comparisons. It was never poor in any of the categories, however. Table 2 shows that the overall assessment value is 2.24, at the high end of the yellow-blue shading. Run 1B, on the other hand, contains blue, yellow, and red. While it was excellent in the MPA ring current categories, it was poor in the plume velocity category and the EUV-derived plasmapause recovery phase category. An overall value of 2.57 for this run puts it at the low end of the yellow in its matrix color assignment. Run 1C is mostly blue, with a little yellow its matrix in Figure 12 (no red, however). This run did well in most of the data categories, and the plume velocity category was the only fair rating among them. Table 2 shows an overall assessment for this run of 1.66, at the low end of the yellow-blue ranking. Run 1D is also dominated by blue, but with a bit more yellow than for run 1D (again, no red). Its accuracy for each category closely matches that of run 1C but occasionally is different, and among these, usually in the negative direction. The overall rating for this run is 1.72, also at the low end of yellow-blue range, but not quite as low as run 1C. Therefore the overall ranking of the runs for storm 1 are as follows: field C is just slightly better than field D, which is much better than field A, which is better than field B.

[87] The storm aggregate results are similar but with a few noteworthy differences. Figure 13 shows that run 2A is

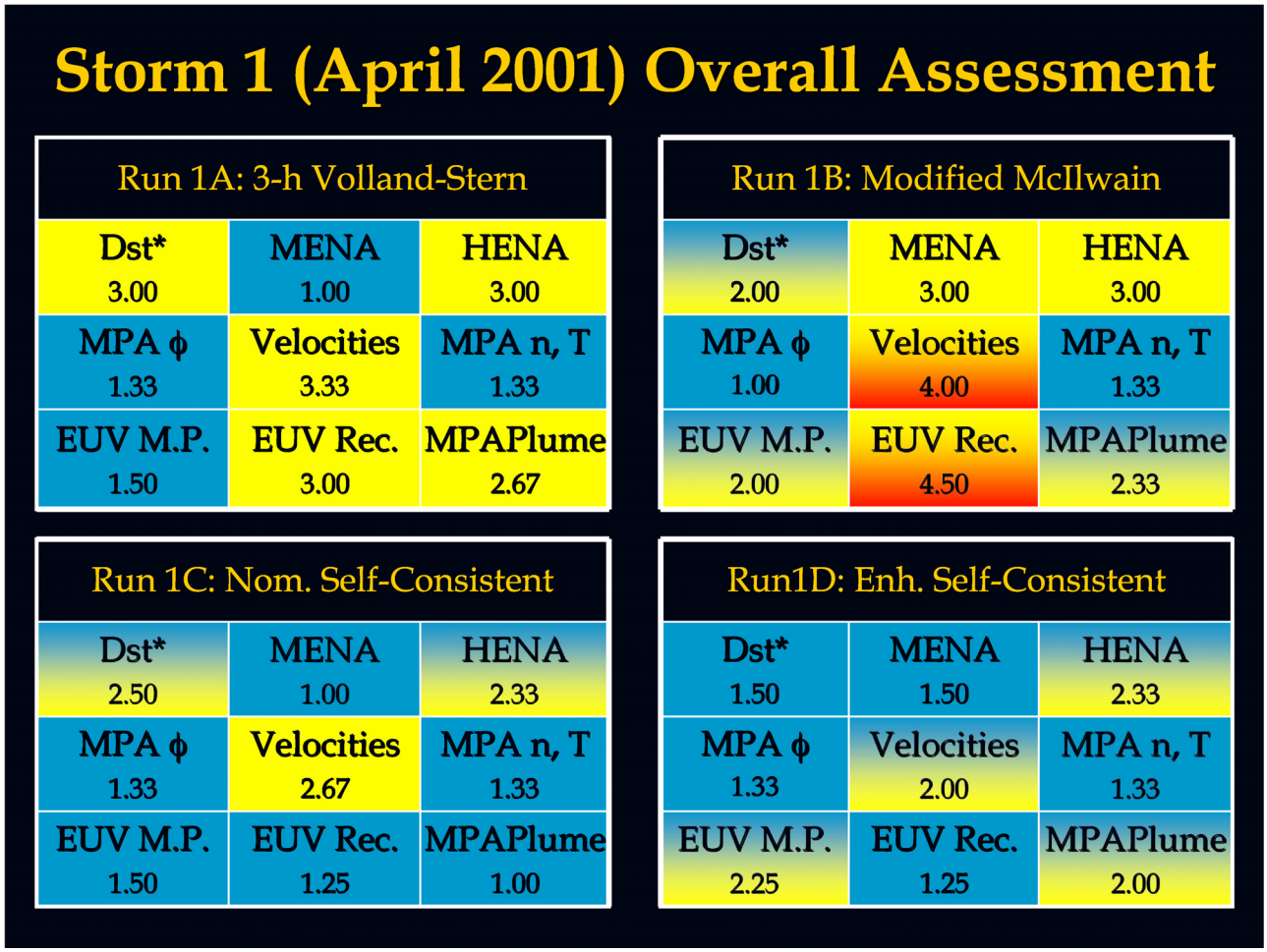

Figure 12. Overall assessments for the simulations of the April 2001 storm. Each of the four runs is shown as a group of nine blocks, with each block representing the average of the comparisons against a particular data set. The numeric value within each block is the quantitative average score for that data set.

mostly blue with some yellow. As with storm 1, there is no red in the matrix for this field description. Table 2 lists the overall assessment for this run as 1.84, near the middle of the yellow-blue rating. Run 2B is again a mixture of all three color assignments. This time, the MENA comparisons were poor, along with both EUV plasmapause categories. None of the categories fell into the solid blue range for this run. Overall, run 2B scored 2.80, which again is at the low end of the yellow classification. Run 2C has roughly equal amounts of yellow and blue in its data category matrix in Figure 13. The *Dst** and EUV main phase categories were only fair, while the MPA flux (DIM) category was excellent. Table 2 gives an overall rating for this run of 2.09, in the middle of the yellow-blue shading but slightly higher than the value for run 2A. Finally, run 2D is again very much like run 2C but with a bit more yellow. Its overall rating of 2.14 places it at the high end of the yellow-blue ranking. So, the overall ranking of the runs for storm 2 is as follows: Field A is better than field C, which is just slightly better than field D, which is much better than field B.

[88] The integrated data comparisons for each storm are quite close to each other. The simulations of storm 1 were slightly better (2.05 compared to 2.22), but this is not a large difference. From storm 1 to storm 2, field A improved its accuracy while the accuracy of the others slightly decreased. The consistency in the data-model comparison accuracy between these two storms indicates that there is not a systematic bias in the results because of the selected storms. That is, it lends validity to generalizing these results for other magnetic storm events.

[89] The final quantities of interest are the averages for each electric field description. Table 2 lists the values, summed over all data sets for both storms, with this overall ranking: field C is just slightly better than field D, which is just slightly better than field A, which is much better than field B. That is, three of the field choices are quite close to each other in total accuracy, while the modified McIlwain field was significantly less accurate. The details of what these overall rankings mean will now be discussed in more detail.

7. Discussion

[90] With the results presented above, it is now possible to address the two questions posed for the Inner Magnetosphere-Storms Assessment Challenge: (1) what level of model sophistication is necessary to obtain a certain accuracy of the result and (2) what is our present understanding

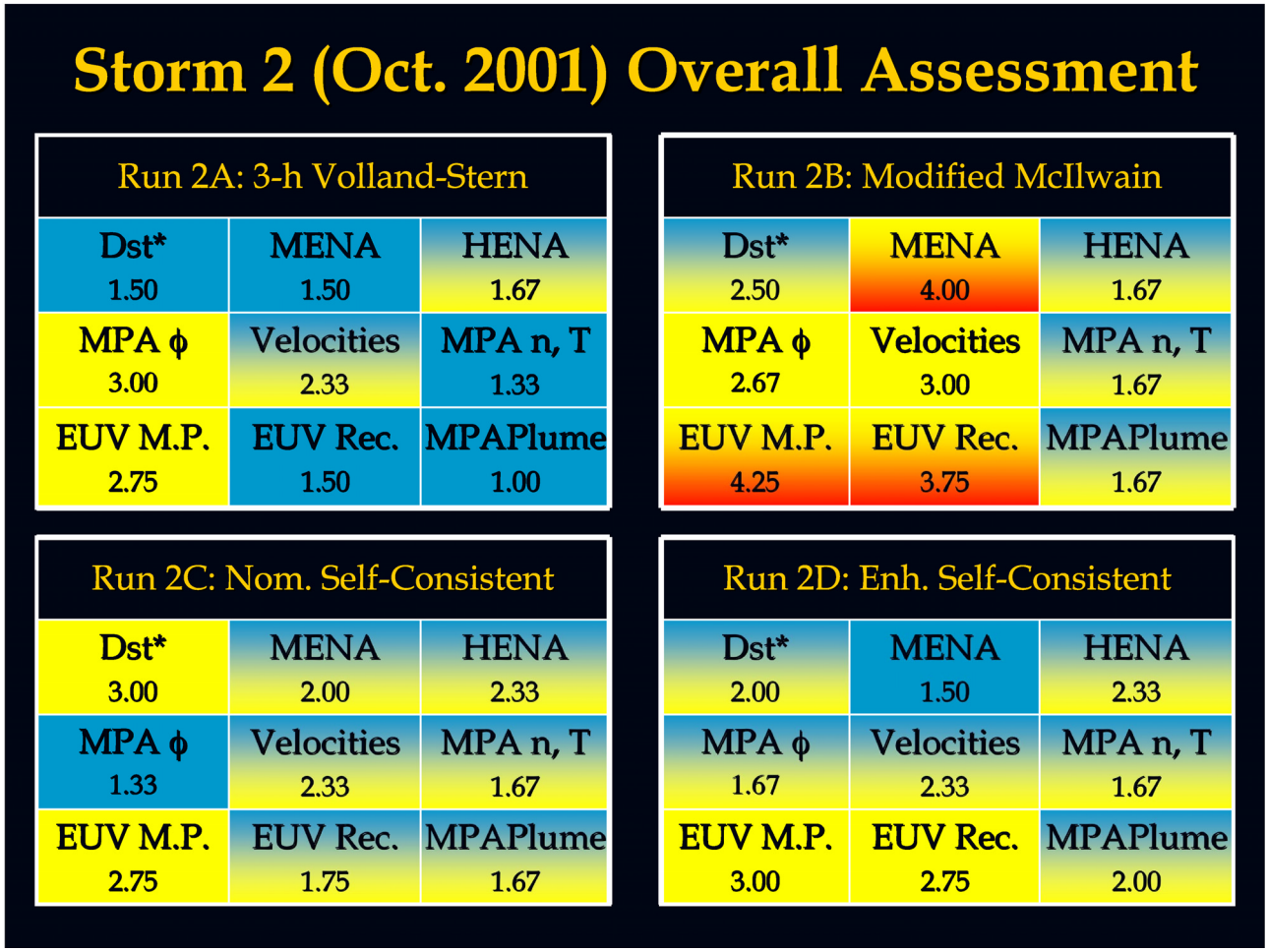

Figure 13. Overall assessments for the simulations of the October 2001 storm. The format is the same as that in Figure 12.

of inner magnetospheric physics? For the present study, these questions can be answered in terms of the inner magnetospheric electric field morphology and dynamics.

7.1. Assessments of the Field Descriptions

[91] The first question can be rephrased as follows: when and where are the systematic strengths and weaknesses of each field description, and when and where do the fields give inconsistent accuracy with data? Let us consider the answer to this question separately for each field description.

[92] Field A, the shielded Volland-Stern electric field driven by the 3-hour *Kp* index, did quite well. It was not that far behind the self-consistent results in its overall assessment score, and it had excellent comparisons against some of the data sets, in particular the MENA peaks and the dayside LANL MPA moments. It was inconsistent with several of the data sets, however. It has several yellow/red or all-red boxes among its individual comparisons, often mixed with all-blue boxes in the same data category for the same storm (the plume velocities for both storms, for instance). Further, it was inconsistent between the storms. The HENA comparisons and the LANL flux comparisons are excellent for one storm and then fair-to-poor for the other. Furthermore, field A performed better against the HENA observations than the LANL fluxes for storm 1, but vice versa for storm 2, so it is even inconsistent in when and where it is inconsistent. A strength of field A is that it seems to properly simulate the main phase. Because this field is a simple two-cell convection pattern and its driver function

Table 2. Overall Assessment

	Sum	Average
	Individual Runs	
Run 1A	20.16	2.24
Run 1B	23.16	2.57
Run 1C	14.91	1.66
Run 1D	15.49	1.72
Run 2A	16.58	1.84
Run 2B	25.18	2.80
Run 2C	18.83	2.09
Run 2D	19.25	2.14
	Integrated By Storm	
Storm 1	73.72	2.05
Storm 2	79.84	2.22
	Integrated By Field	
Field A	36.74	2.04
Field B	48.34	2.69
Field C	33.74	1.87
Field D	34.74	1.93

does not change rapidly with time, this conclusion implies that the true electric field in the inner magnetosphere during the main phase of storms is dominated by the large-scale convection potential. That is, the modifications to the convection pattern because of closure of the partial ring current through the ionosphere are perhaps not critical for obtaining the large-scale plasma dynamics of storm main phases. The results also imply that this simple, 30-year-old electric field model is still a useful descriptor for the inner magnetosphere.

[93] Field B, the McIlwain E5D model with the modification to use a cross polar cap potential input parameter, did not do that well compared to the other selected field models. Its strengths include reproducing the dayside hot ion fluxes and moments, and it also had reasonable success in capturing the *Dst** time series and the location of the plasmaspheric drainage plume. It was not good at simulating the morphology of the low-energy ring current as seen by MENA, and it had mixed success in reproducing the high-energy observations of HENA. Where it truly failed was the plasmapause location across the morningside of the Earth. This implies that the strong dawnside, eastward flow present in this field description is not a particularly realistic feature. So, this field is adequate for modeling some features of inner magnetospheric plasma dynamics, such as the total energy content of the ring current or for afternoon/duskside plasma features, but it is not the best available electric field model for the storm time inner magnetosphere.

[94] Field C, the self-consistent electric field description with the nominal setting for the relationship between the ionospheric conductance and the ring current FACs, was the best overall model among those tested in this study. In the individual data-model comparisons, it had no all-red color assignments and only had a few yellow-red assignments in storm 2 (none for storm 1). That is, it consistently performed well against the broad collection of selected data sets. It did better at reproducing the *Dst** minimum than it did reproducing the entire *Dst** time series, the latter of which it consistently underpredicted the magnitude of the magnetic depression. It was very good at matching the MENA and HENA observations, except for the highest-energy channel of HENA used in this study (60–119 keV), again in which it produced consistently lower ENA fluxes than those observed. It was excellent at both the dayside LANL fluxes and moments, and it was also excellent at simulating the plasmaspheric drainage plume location. It was consistently good at reproducing the plasmapause shape and dynamics as observed by EUV, except perhaps in the premidnight sector, where it was only fair, on average. Like all of the other field descriptions, it was consistently low compared to the observed velocities within the plasmaspheric drainage plume, but it was closer to the observed values than were the analytical field models. In general, there was no plasmaspheric or ring current data set for which this field produced poor data-model comparisons. These results lead to the conclusion that this electric field description should be the field of choice for inner magnetospheric storm time simulations.

[95] Field D, the self-consistent electric field with double the ionospheric conductance for a given FAC magnitude (relative to field C), performed quite similarly to the nominal self-consistent electric field. It also had no all-red individual data-model comparison assignments and only three yellow-red colorings in the plasmasphere comparisons for storm 2 (none for storm 1). Even though it scored better than field C in a few areas (most notably in reproducing *Dst**), field C consistently outperformed field D with slightly better overall ratings for both storms. The plasmaspheric data-model comparisons are the ones where field D was not quite as good as field C. So, all of the comments in the paragraph above also apply for this field description, but if forced to choose between the two models, the nominal settings are better than the enhanced conductance settings.

7.2. Assessment of Our Understanding of the Inner Magnetospheric Electric Field

[96] With respect to this study, the second question posed for the IMSAC can be rewritten like this: what is known about the inner magnetospheric electric field pattern, and what is still left to discover about this field? The results of this study suggest that sophisticated electric field models (that is, beyond a formulaic empirical description) are not needed to reproduce the bulk quantities of the inner magnetospheric plasma distribution, specifically *Dst** (as simulated by the ring current total energy content using the Dessler-Parker-Sckopke relation). Both of the analytical models demonstrated success at simulating the peaks and the time series of this index. However, the comparison was only good for one of the storms (field A did well with storm 2, while field B did well with storm 1). That is, they can be useful in obtaining this integrated quantity, but their accuracy is inconsistent and caution should be used. In addition, matching *Dst** was not a guarantee that the details of the result are also correct. For instance, the Volland-Stern field did very well at simulating the *Dst** quantities for storm 2 but then was poor at predicting the DIM location and only fair at reproducing the main phase plasmapause location and dynamics. Therefore it is concluded that the large-scale convection strength is the primary driver of the bulk plasma properties of the inner magnetosphere (in terms of electric field control of these values), but this quantity alone is not enough to consistently reproduce the details of the storm time plasma distribution.

[97] The results imply that the electric field features of the self-consistent potential description are much better at consistently simulating these small-scale details of the plasmasphere and ring current than were the simplistic analytical models. The biggest distinguishing features of these fields is the midnight potential well associated with the eastward end of the storm time partial ring current peak and the corresponding (but smaller) potential peak near dusk. The former structure distorts the equipotential contours into the morning sector (see the discussion by *Fok et al.* [2003]), while the latter structure is responsible for the formation of the SAPS [e.g., *Foster and Burke*, 2002; *Foster and Vo*, 2002]. In addition, the phenomena of undershielding following convection enhancements and overshielding following convection reductions are standard features of the self-consistent models (while they are not well represented in the analytical models). Therefore it is concluded that these features of the inner magnetospheric electric field morphology are critical for consistently good

accuracy in simulations of the storm time plasmasphere and ring current.

[98] Note that all of the self-consistent electric field simulations conducted for this study used fixed FAC-to-Σ relationships for the ionospheric auroral oval conductance pattern. That is, the oval varied in time, but how it varied with respect to the RAM-generated ionospheric inputs was held constant throughout each simulation. It was shown above that, at certain times and places, the enhanced conductance results were closer to the observations than the nominal conductance results. Therefore time-dependent settings in the electric field calculation, rather than the fixed values used in the current simulations, are expected to greatly improve the ability of models to track the observations over the course of the storms. How these relationships vary throughout a storm is still an unresolved issue.

[99] Small-scale potential structures in the inner magnetosphere, a phenomenon that often arises in the self-consistent solutions, is something that still needs to be observationally confirmed. *Liemohn and Brandt* [2005] showed that these small-scale features cannot be detected by the IMAGE-HENA instrument, and the present study has not resolved this debate. Therefore additional evidence must be collected to substantiate their existence. Upcoming scientific satellite missions such as TWINS and the Radiation Belt Storm Probes offer the best hope for answering this question.

[100] Another question that remains unresolved, and indeed unaddressed in this study, is the observed subcorotation of the plasmasphere [e.g., *Burch et al.*, 2004; *Gallagher et al.*, 2005]. Several mechanisms have been proposed, but it still remains to be proven which of these processes is the dominant one responsible for the effect.

[101] Yet another mystery is sawtooth oscillation events [*Henderson et al.*, 2006; *Clauer et al.*, 2006; *Borovsky et al.*, 2006]. These are times of strong, quasi-periodic stretching and sudden dipolarization of the inner magnetospheric magnetic field, usually occurring during intense magnetic storms. *Liemohn et al.* [2006] showed that self-consistent ring current simulations have difficulty reproducing the *Dst** time series during these events, even though they seem to match the ENA flux observations quite well. The true nature of the inner magnetosphere during these intervals, particularly the ring current response to this peculiar driving condition, is still an unresolved issue.

[102] Finally, a topic that has received some attention lately is the nonlinear feedback of the ring current strength on the electric field. *Kozyra and Liemohn* [2003] argued that the electric field is only half of the ring current input equation, and the other half is the plasma sheet density. *Ebihara et al.* [2005] examined the influence of plasma sheet density on the self-consistent development of the ring current, concluding that there is a nonlinear relationship because of a negative feedback. That is, the formation of the midnight potential well hinders additional ring current growth. This was also the conclusion of *Liemohn and Brandt* [2005], who found that the self-consistent electric field breaks up the inner magnetospheric hot ion pressure peak and reduces the intensity of the ring current. The plasma sheet temperature is also a factor. Using a two-cell convection model, *Ebihara and Ejiri* [2000] found that there is an optimum temperature for maximum ring current development (because of the competing terms in the ion drift equation), and *Garner* [2003] also found a plasma sheet temperature dependence on the self-consistent development of the ring current. There is still work to be done here, though. In particular, the plasma sheet characteristics vary with storm size and solar cycle phase [*Denton et al.*, 2005a; *Zhang et al.*, 2006], and the reasons for this are largely unknown. This is still an area of active research with many promising studies already underway.

8. Summary and Conclusions

[103] Several plasmasphere-ring current simulations using different electric field descriptions were conducted in order to assess the accuracy of these fields and to quantify our knowledge of inner magnetospheric storm time dynamics. Four electric field descriptions were chosen for this study: the shielded Volland-Stern field, the modified McIlwain field, a nominal self-consistent field, and an enhanced conductance self-consistent field. Two magnetic storms were simulated: those on 22 April 2001 and 21–23 October 2001. A large number of plasmaspheric and ring current data sets were used to quantify the accuracy of the simulations. The assessments of the four selected fields are as follows:

[104] 1. The shielded Volland-Stern electric field performed quite well in reproducing the features of a number of diverse data sets. In fact, for storm 2, its data-model comparisons were better than the self-consistent models in many categories. The results were often inconsistent, though.

[105] 2. The modified McIlwain field was noticeably worse than the other fields in many categories, but it was fairly good at reproducing a few key data sets, most importantly *Dst**. This field had the most comparisons ranked in the poor assessment categories, however, and it is not recommended for widespread usage unless only those certain features for which this field did well are of interest.

[106] 3. The nominal self-consistent electric field was the best at reproducing the selected data. Moreover, it consistently did well, with very few bad data-model comparisons. This field is recommended as the standard field for inner magnetospheric storm simulations.

[107] 4. The enhanced-conductance self-consistent electric field was also very good and very consistent in reproducing the wide variety of data. The relatively enhanced conductance decreased the strength of the inner magnetospheric shielding potential, therefore allowing more penetration of the large-scale convection field and thus more particle injection and flow-through. It outperformed the nominal-setting field in matching the properties of the *Dst** index, but it was worse at capturing the location and dynamics of the plasmapause. It is also recommended for storm simulations, but given the choice, the nominal settings are better.

[108] Note that two large assumptions in the modeling approach add a caveat to these assessments. One limiting factor is the use of a static dipole magnetic field, and recently computational studies have shown that the ring current's distortion of the magnetic field can significantly impact the development of the storm time ring current [e.g., *Zaharia et al.*, 2005, 2006; *Chen et al.*, 2006]. The second

is the use of the *Young et al.* [1982] formulas to specify the hot ion composition entering the inner magnetosphere from the near-Earth plasma sheet. Ion composition can influence the loss rate of the ring current.

[109] From these assessments, it is possible to write a list of unresolved issues regarding the inner magnetospheric electric field, as discussed in section 7.2, above: (1) time-dependent settings in the electric field calculation, rather than the fixed values used in the current simulations, (2) quantification of overshielding and undershielding levels against solar wind and/or geophysical parameters, (3) confirmation of the existence of any small-scale potential structures, (4) resolution of the subcorotation drift speed mechanism, (5) unraveling the mystery of global sawtooth oscillation events, (6) improvement of our understanding of the nonlinear coupling between the ring current, plasmasphere, and midlatitude ionosphere. While this is not an exhaustive list of issues, it can be used as a starting point from which to continue our exploration and quantification of the inner magnetospheric electric field.

[110] In conclusion, the major findings regarding the morphology and dynamics of the storm time inner magnetospheric electric field can be summarized as follows: (1) Simple analytical field models are adequate for reproducing the large-scale morphology and bulk parameters of the ring current and plasmasphere. However, the accuracy is not consistent, and the results for each storm must be scrutinized and validated. (2) Typical features of the self-consistent electric field models, such as the midnight potential well and the duskside SAPS, are necessary for consistently accurate results for the plasmasphere and ring current across a broad range of dynamical features of these populations.

[111] **Acknowledgments.** The authors would like to thank the sources of funding for this study: NASA grants NAG5-12722, NAG5-10297, NAG-10850, NAG-12772, NNG05GJ89G, NNG06GE02G, and NNG05GM48G; and NSF grants ATM-0302529, ATM-0090165, ATM-0302529, ATM-0402163, and ATM-0455727. The authors would also like to thank all of their data providers who made the ring current simulations possible, especially G. D. Reeves at the Los Alamos National Laboratory for the SOPA data, the Kyoto World Data Center for the *Kp* and *Dst* index, and CDAWeb for allowing access to the level-2 plasma and magnetic field data of the ACE spacecraft (and D. J. McComas and N. Ness for providing their data to CDAWeb).

[112] Amitava Bhattacharjee thanks James Burch and another reviewer for their assistance in evaluating this paper.

References

Bame, S. J., et al. (1993), Magnetospheric plasma analyzer for spacecraft with constrained resources, *Rev. Sci. Instrum.*, *64*, 1026.

Belian, R. D., G. R. Gisler, T. Cayton, and R. Christensen (1992), High-Z energetic particles at geosynchronous orbit during the great solar proton event series of October 1989, *J. Geophys. Res.*, *97*, 16,897.

Boonsiriseth, A., R. M. Thorne, G. Lu, V. K. Jordanova, M. F. Thomsen, D. M. Ober, and A. J. Ridley (2001), A semiempirical equatorial mapping of AMIE convection electric potentials (MACEP) for the January 10, 1997, magnetic storm, *J. Geophys. Res.*, *106*, 12,903.

Borovsky, J. E., M. F. Thomsen, and D. J. McComas (1997), The superdense plasma sheet: Plasmaspheric origin, solar wind origin, or ionospheric origin?, *J. Geophys. Res.*, *102*, 22,089.

Borovsky, J. E., R. J. Nemzek, C. W. Smith, R. M. Skoug, and C. R. Clauer (2006), The solar-wind driving of global sawtooth oscillations and periodic substorms: What determines the periodicity?, *Ann. Geophys.*, in press.

Brandt, P. C., S. Ohtani, D. G. Mitchell, R. Demajistre, and E. C. Roelof (2002a), ENA observations of a global substorm growthphase dropout in the nightside magnetosphere, *Geophys. Res. Lett.*, *29*(20), 1962, doi:10.1029/2002GL015057.

Brandt, P. C., R. Demajistre, E. C. Roelof, S. Ohtani, D. G. Mitchell, and S. Mende (2002b), IMAGE/high-energy energetic neutral atom: Global energetic neutral atom imaging of the plasma sheet and ring current during substorms, *J. Geophys. Res.*, *107*(A12), 1454, doi:10.1029/2002JA009307.

Brandt, P. C., S. Ohtani, D. G. Mitchell, M.-C. Fok, E. C. Roelof, and R. Demajistre (2002c), Global ENA observations of the storm mainphase ring current: Implications for skewed electric fields in the inner magnetosphere, *Geophys. Res. Lett.*, *29*(20), 1954, doi:10.1029/2002GL015160.

Brandt, P. C., D. G. Mitchell, Y. Ebihara, B. R. Sandel, E. C. Roelof, J. L. Burch, and R. Demajistre (2002d), Global IMAGE/HENA observations of the ring current: Examples of rapid response to IMF and ring current-plasmasphere interaction, *J. Geophys. Res.*, *107*(A11), 1359, doi:10.1029/2001JA000084.

Brandt, P. C., J. Goldstein, B. J. Anderson, H. Korth, T. J. Immel, E. C. Roelof, R. DeMajistre, D. G. Mitchell, and B. R. Sandel (2005), On the relation between electric fields in the inner magnetosphere, ring current, aruroral conductance and plasmapause motion, in *Global Interactions of the Coupled Inner Magnetosphere*, *Geophys. Monogr. Ser.*, edited by J. L. Burch, AGU, Washington, D. C., in press.

Burch, J. L., J. Goldstein, and B. R. Sandel (2004), Cause of plasmasphere corotation lag, *Geophys. Res. Lett.*, *31*, L05802, doi:10.1029/2003GL019164.

Carovillano, R. L., and G. L. Siscoe (1973), Energy and momentum theorems in magnetospheric processes, *Rev. Geophys. Space Phys.*, *11*, 289.

Carpenter, D. L. (1962), New experimental evidence of effect of magnetic storms on magnetosphere, *J. Geophys. Res.*, *67*, 135.

Carpenter, D. L. (1963), Whistler evidence of a "knee" in the magnetospheric ionization density profile, *J. Geophys. Res.*, *68*, 1675.

Chandler, M. O., and T. E. Moore (2003), Observations of the geopause at the equatorial magnetopause: Density and temperature, *Geophys. Res. Lett.*, *30*(16), 1869, doi:10.1029/2003GL017611.

Chappell, C. R., K. K. Harris, and G. W. Sharp (1970), The morphology of the bulge region of the plasmasphere, *J. Geophys. Res.*, *75*, 3848.

Chen, M. W., M. Schulz, G. Lu, and L. R. Lyons (2003), Quasi-steady drift paths in a model magnetosphere with AMIE electric field: Implications for ring current formation, *J. Geophys. Res.*, *108*(A5), 1180, doi:10.1029/2002JA009584.

Chen, M. W., S. Liu, M. Schulz, J. L. Roeder, and L. R. Lyons (2006), Magnetically self-consistent ring current simulations during the 19 October 1998 storm, *J. Geophys. Res.*, doi:10.1029/2006JA011620, in press.

Clauer, C. R., X. Cai, D. Welling, A. DeJong, and M. G. Henderson (2006), Characterizing the April 18, 2002 storm-time sawtooth events using ground magnetic data, *J. Geophys. Res.*, *111*, A04S90, doi:10.1029/2005JA011099.

Denton, M. H., M. F. Thomsen, H. Korth, S. Lynch, J.-C. Zhang, and M. W. Liemohn (2005a), Bulk plasma properties at geosynchronous orbit, *J. Geophys. Res.*, *110*, A07223, doi:10.1029/2004JA010861.

Denton, M. H., V. K. Jordanova, M. G. Henderson, R. M. Skoug, M. F. Thomsen, C. J. Pollock, S. Zaharia, and H. O. Funsten (2005b), Storm-time plasma signatures observed by IMAGE/MENA and comparison with a global physics-based model, *Geophys. Res. Lett.*, *32*, L17102, doi:10.1029/2005GL023353.

Dessler, A. J., and E. N. Parker (1959), Hydromagnetic theory of geomagnetic storms, *J. Geophys. Res.*, *64*, 2239.

Dungey, J. W. (1963), The loss of Van Allen electrons due to whistlers, *Planet. Space Sci.*, *11*, 591.

Ebihara, Y., and M. Ejiri (2000), Simulation study on fundamental properties of the storm-time ring current, *J. Geophys. Res.*, *105*, 15,843.

Ebihara, Y., and M.-C. Fok (2004), Postmidnight storm-time enhancement of tens-of-keV proton flux, *J. Geophys. Res.*, *109*, A12209, doi:10.1029/2004JA010523.

Ebihara, Y., M.-C. Fok, R. A. Wolf, T. J. Immel, and T. E. Moore (2004), Influence of ionospheric conductivity on the ring current, *J. Geophys. Res.*, *109*, A08205, doi:10.1029/2003JA010351.

Ebihara, Y., M-C. Fok, R. A. Wolf, M. F. Thomsen, and T. E. Moore (2005), Nonlinear impact of plasma sheet density on the storm-time ring current, *J. Geophys. Res.*, *110*, A02208, doi:10.1029/2004JA010435.

Ejiri, M. (1978), Trajectory traces of charged particles in the magnetosphere, *J. Geophys. Res.*, *83*, 4798.

Elphic, R. C., M. F. Thomsen, and J. E. Borovsky (1997), The fate of the outer plasmasphere, *Geophys. Res. Lett.*, *24*, 365.

Fok, M-C., J. U. Kozyra, A. F. Nagy, C. E. Rasmussen, and G. V. Khazanov (1993), A decay model of equatorial ring current and the associated aeronomical consequences, *J. Geophys. Res.*, *98*, 19,381.

Fok, M.-C., R. A. Wolf, R. W. Spiro, and T. E. Moore (2001), Comprehensive computational model of the earth's ring current, *J. Geophys. Res.*, *106*, 8417.

Fok, M.-C., et al. (2003), Global ENA image simulations, *Space Sci. Rev.*, *109*, 77.

Foster, J. C., and W. J. Burke (2002), SAPS: A new categorization of subauroral electric fields, *Eos Trans. AGU*, *83*(36), 393.

Foster, J. C., and H. B. Vo (2002), Average characteristics and activity dependence of the subauroral polarization stream, *J. Geophys. Res.*, *107*(A12), 1475, doi:10.1029/2002JA009409.

Foster, J. C., P. J. Erickson, A. J. Coster, J. Goldstein, and F. J. Rich (2002), Ionospheric signatures of plasmaspheric tails, *Geophys. Res. Lett.*, *29*(13), 1623, doi:10.1029/2002GL015067.

Freeman, J. W., Jr., H. K. Hills, T. W. Hill, P. H. Reiff, and D. A. Hardy (1977), Heavy ion circulation in the Earth's magnetosphere, *Geophys. Res. Lett.*, *4*, 195.

Friedel, R. H. W., H. Korth, M. G. Henderson, M. F. Thomsen, and J. D. Scudder (2001), Plasma sheet access to the inner magnetosphere, *J. Geophys. Res.*, *106*, 5845.

Gallagher, D. L., M. L. Adrian, and M. W. Liemohn (2005), The origin and evolution of deep plasmaspheric notches, *J. Geophys. Res.*, *110*, A09201, doi:10.1029/2004JA010906.

Ganushkina, N. Y., et al. (2000), Entry of plasma sheet particles into the inner magnetosphere as observed by Polar/CAMMICE, *J. Geophys. Res.*, *105*, 25,205.

Garner, T. W. (2003), Numerical experiments on the inner magnetospheric electric field, *J. Geophys. Res.*, *108*(A10), 1373, doi:10.1029/2003JA010039.

Goldstein, J., R. W. Spiro, P. H. Reiff, R. A. Wolf, B. R. Sandel, J. W. Freeman, and R. L. Lambour (2002), IMF-driven overshielding electric field and the origin of the plasmaspheric shoulder on May 24, 2000, *Geophys. Res. Lett.*, *29*(16), 1819, doi:10.1029/2001GL014534.

Goldstein, J., B. R. Sandel, M. R. Hairston, and P. H. Reiff (2003), Control of plasmaspheric dynamics by both convection and subauroral polarization stream, *Geophys. Res. Lett.*, *30*(24), 2243, doi:10.1029/2003GL018390.

Goldstein, J., R. A. Wolf, B. R. Sandel, and P. H. Reiff (2004), Electric fields deduced from plasmapause motion in IMAGE EUV images, *Geophys. Res. Lett.*, *31*, L01801, doi:10.1029/2003GL018797.

Goldstein, J., J. L. Burch, B. R. Sandel, S. B. Mende, P. C. Brandt, and M. R. Hairston (2005), Coupled response of the inner magnetosphere and ionosphere on 17 April 2002, *J. Geophys. Res.*, *110*, A03205, doi:10.1029/2004JA010712.

Grafe, A. (1999), Are our ideas about Dst correct?, *Ann. Geophys.*, *17*, 1–10.

Green, J. C., and M. G. Kivelson (2001), A tale of two theories: How the adiabatic response and ULF waves affect relativistic electrons, *J. Geophys. Res.*, *106*, 25,777.

Greenspan, M. E., and D. C. Hamilton (2000), A test of the Dessler-Parker-Sckopke relation during magnetic storms, *J. Geophys. Res.*, *105*, 5419.

Gussenhoven, M. S., D. A. Hardy, and W. J. Burke (1981), DMSP/F2 electron observations of equatorward auroral boundaries and their relationship to magnetospheric electric fields, *J. Geophys. Res.*, *86*, 768.

Gussenhoven, M. S., D. A. Hardy, and N. Heinemann (1983), Systematics of the equatorward diffuse auroral boundary, *J. Geophys. Res.*, *88*, 5692.

Henderson, M. G., et al. (1997), First energetic neutral atom images from Polar CEPPAR/IPS, *Geophys. Res. Lett.*, *24*, 1167.

Henderson, M. G., M. F. Thomsen, R. Skoug, M. H. Denton, R. Harper, H. O. Funsten, and C. J. Pollock (2005), Calculation of IMAGE/MENA geometric factors and conversion of images to units of integral and differential flux, *Rev. Sci. Instr.*, *76*, 043303, doi:10.1063/1.1884190.

Henderson, M. G., G. D. Reeves, R. Skoug, M. F. Thomsen, M. H. Denton, S. B. Mende, T. J. Immel, P. C. Brandt, and H. J. Singer (2006), Magnetospheric and auroral activity during the 18 April 2002 sawtooth event, *J. Geophys. Res.*, *111*, A01S90, doi:10.1029/2005JA011111.

Hudson, M. K., V. A. Marchenko, I. Roth, M. Temerin, J. B. Blake, and M. S. Gussenhoven (1998), Radiation belt formation during storm sudden commencements and loss during main phase, *Adv. Space Res.*, *21*(4), 597.

Jaggi, R. K., and R. A. Wolf (1973), Self-consistent calculation of the motion of a sheet of ions in the magnetosphere, *J. Geophys. Res.*, *78*, 2842.

Jordanova, V. K., and Y. Miyoshi (2005), Relativistic model of ring current and radiation belt ions and electrons: Initial results, *Geophys. Res. Lett.*, *32*, L14104, doi:10.1029/2005GL023020.

Jordanova, V. K., J. U. Kozyra, G. V. Khazanov, A. F. Nagy, C. E. Rasmussen, and M.-C. Fok (1994), A bounce-averaged kinetic model of the ring current ion population, *Geophys. Res. Lett.*, *21*, 2785.

Jordanova, V. K., L. M. Kistler, J. U. Kozyra, G. V. Khazanov, and A. F. Nagy (1996), Collisional losses of ring current ions, *J. Geophys. Res.*, *101*, 111.

Jordanova, V. K., L. M. Kistler, C. J. Farrugia, and R. B. Torbert (2001), Effects of inner magnetospheric convection on ring current dynamics: March 10–12, 1998, *J. Geophys. Res.*, *106*, 29,705.

Jordanova, V. K., A. Boonsiriseth, R. M. Thorne, and Y. Dotan (2003), Ring current asymmetry from global simulations using a high-resolution electric field model, *J. Geophys. Res.*, *108*(A12), 1443, doi:10.1029/2003JA009993.

Jorgensen, A. M., M. G. Henderson, E. C. Roelof, G. D. Reeves, and H. E. Spence (2001), Charge exchange contribution to the decay of the ring current, measured by energetic neutral atoms (ENAs), *J. Geophys. Res.*, *106*, 1931.

Jorgensen, A. M., H. E. Spence, W. J. Hughes, and H. J. Singer (2004), A statistical study of the global structure of the ring current, *J. Geophys. Res.*, *109*, A12204, doi:10.1029/2003JA010090.

Kennel, C. F., and H. E. Petschek (1966), Limit on stably trapped particle fluxes, *J. Geophys. Res.*, *71*, 1.

Khazanov, G. V., M. W. Liemohn, T. S. Newman, M.-C. Fok, and R. W. Spiro (2003), Self-consistent magnetosphere-ionosphere coupling: Theoretical studies, *J. Geophys. Res.*, *108*(A3), 1122, doi:10.1029/2002JA009624.

Khazanov, G. V., M. W. Liemohn, T. S. Newman, M.-C. Fok, and A. J. Ridley (2004a), Magnetospheric convection electric field dynamics and stormtime particle energization: Case study of the magnetic storm of 4 May 1998, *Ann. Geophys.*, *22*, 497.

Khazanov, G. V., M. W. Liemohn, M.-C. Fok, T. S. Newman, and A. J. Ridley (2004b), Stormtime particle energization with AMIE potentials, *J. Geophys. Res.*, *109*, A05209, doi:10.1029/2003JA010186.

Korth, H., M. F. Thomsen, J. E. Borovsky, and D. J. McComas (1999), Plasma sheet access to geosynchronous orbit, *J. Geophys. Res.*, *104*, 25,047.

Kozyra, J. U., and M. W. Liemohn (2003), Ring current energy input and decay, *Space Sci. Rev*, *109*, 105.

Le, G., C. T. Russell, and K. Takahashi (2004), Morphology of the ring current derived from magnetic field observations, *Ann. Geophys.*, *22*, 1267.

Liemohn, M. W. (2003), Yet another caveat to the Dessler-Parker-Sckopke relation, *J. Geophys. Res.*, *108*(A6), 1251, doi:10.1029/2003JA009839.

Liemohn, M. W., and P. C. Brandt (2005), Small-scale structure in the stormtime ring current, *Inner Magnetosphere Interactions: New Perspectives from Imaging*, *Geophys. Monogr. Ser.*, vol. 159, edited by J. L. Burch, M. Schulz, and H. Spence, p. 167, AGU, Washington, D. C.

Liemohn, M. W., J. U. Kozyra, V. K. Jordanova, G. V. Khazanov, M. F. Thomsen, and T. E. Cayton (1999), Analysis of early phase ring current recovery mechanisms during geomagnetic storms, *Geophys. Res. Lett.*, *25*, 2845.

Liemohn, M. W., J. U. Kozyra, M. F. Thomsen, J. L. Roeder, G. Lu, J. E. Borovsky, and T. E. Cayton (2001a), Dominant role of the asymmetric ring current in producing the stormtime Dst*, *J. Geophys. Res.*, *106*, 10,883.

Liemohn, M. W., J. U. Kozyra, C. R. Clauer, and A. J. Ridley (2001b), Computational analysis of the near-Earth magnetospheric current system, *J. Geophys. Res.*, *106*, 29,531.

Liemohn, M. W., A. J. Ridley, D. L. Gallagher, D. M. Ober, and J. U. Kozyra (2004), Dependence of plasmaspheric morphology on the electric field description during the recovery phase of the April 17, 2002 magnetic storm, *J. Geophys. Res.*, *109*(A3), A03209, doi:10.1029/2003JA010304.

Liemohn, M. W., A. J. Ridley, P. C. Brandt, D. L. Gallagher, J. U. Kozyra, D. G. Mitchell, E. C. Roelof, and R. DeMajistre (2005), Parametric analysis of nightside conductance effects on inner magnetospheric dynamics for the 17 April 2002 storm, *J. Geophys. Res.*, *110*, A12S22, doi:10.1029/2005JA011109.

Liemohn, M. W., J. U. Zozyra, A. J. Ridley, M. F. Thomsen, M. G. Henderson, P. C. Brandt, and D. G. Mitchell (2006), Modeling the ring-current response to a sawtooth oscillation event, *J. Atmos. Sol. Terr. Phys.*, in press.

Lui, A. T. Y. (2003), Inner magnetospheric plasma pressure distribution and its local time asymmetry, *Geophys. Res. Lett.*, *30*(16), 1846, doi:10.1029/2003GL017596.

Lui, A. T. Y., R. M. McEntire, M. Nosé, and D. J. Williams (2001a), Composition of energetic neutral atoms during a storm main phase, *Geophys. Res. Lett.*, *28*(7), 1363.

Lui, A. T. Y., R. M. McEntire, and K. B. Baker (2001b), A new insight on the cause of magnetic storms, *Geophys. Res. Lett.*, *28*(17), 3413.

Lyons, L. R., and D. J. Williams (1984), *Quantitative Aspects of Magnetospheric Physics*, Springer, New York.

Maynard, N. C., and A. J. Chen (1975), Isolated cold plasma regions: Observations and their relation to possible production mechanisms, *J. Geophys. Res.*, *80*, 1009.

McComas, D. J., S. J. Bame, P. Barker, W. C. Feldman, J. L. Phillips, P. Riley, and J. W. Griffee (1998), Solar wind electron proton alpha monitor (SWEPAM) for the Advanced Composition Explorer, *Space Sci. Rev.*, *86*, 563.

McIlwain, C. E. (1986), A *Kp* dependent equatorial electric field model, *Adv. Space Res.*, *6*, 187.
Mitchell, D. G., et al. (2000), High energy neutral atom (HENA) imager for the IMAGE mission, *Space Sci. Rev.*, *91*, 67.
Mitchell, D. G., K. C. Hsieh, C. C. Curtis, D. C. Hamilton, H. D. Voss, E. C. Roelof, and P. Brandt (2001), Imaging two geomagnetic storms in energetic neutral atoms, *Geophys. Res. Lett.*, *28*, 1151.
Mitchell, D. G., P. C. Brandt, E. C. Roelof, D. C. Hamilton, K. C. Retterer, and S. Mende (2003), Global imaging of O^+ from IMAGE/HENA, *Space Sci. Rev.*, *109*, 63.
Ober, D. M., J. L. Horwitz, M. F. Thomsen, R. C. Elphic, D. J. McComas, R. D. Belian, and M. B. Moldwin (1997a), Premidnight plasmaspheric "plumes", *J. Geophys. Res.*, *102*, 11,325.
Ober, D. M., J. L. Horwitz, and D. L. Gallagher (1997b), Formation of density troughs embedded in the outer plasmasphere by subauroral ion drift events, *J. Geophys. Res.*, *102*, 14,595.
Park, C. G., and D. L. Carpenter (1970), Whistler evidence of large-scale electron-density irregularities in plasmasphere, *J. Geophys. Res.*, *75*, 3825.
Parker, E. N., and H. A. Stewart (1967), Nonlinear inflation of a magnetic dipole, *J. Geophys. Res.*, *72*, 5287.
Pollock, C. J., et al. (2000), Medium energy neutral atom (MENA) imager for the IMAGE mission, *Space Sci. Rev.*, *91*, 113.
Pollock, C. J., et al. (2001), Initial Medium Energy Neutral Atom (MENA) images of Earth's magnetosphere during substorms and storm-time, *Geophys. Res. Lett.*, *28*, 1147.
Pollock, C. J., et al. (2003), The role and contributions of energetic neutral atom (ENA) imaging in magnetospheric substorm research, *Space Sci. Rev.*, *109*, 155.
Rairden, R. L., L. A. Frank, and J. D. Craven (1986), Geocoronal imaging with Dynamics Explorer, *J. Geophys. Res.*, *91*, 13,613.
Reeves, G. D., and M. G. Henderson (2001), The storm-substorm relationship: Ion injections in geosynchronous measurements and composite energetic neutral atom images, *J. Geophys. Res.*, *106*, 5833.
Richmond, A. D., and Y. Kamide (1988), Mapping electrodynamic features of the high-latitude ionosphere from localized observations: Technique, *J. Geophys. Res.*, *93*, 5741.
Ridley, A. J., and M. W. Liemohn (2002), A model-derived description of the penetration electric field, *J. Geophys. Res.*, *107*(A8), 1151, doi:10.1029/2001JA000051.
Ridley, A. J., T. I. Gombosi, and D. L. De Zeeuw (2004), Ionospheric control of the magnetosphere: Conductance, *Ann. Geophys.*, *22*, 567.
Rowland, D., and J. R. Wygant (1998), The dependence of the large scale electric field in the inner magnetosphere on magnetic activity, *J. Geophys. Res.*, *103*, 14,959.
Sandel, B. R., et al. (2000), The extreme ultraviolet imager investigation for the IMAGE mission, *Space Sci. Rev.*, *91*, 197.
Sandel, B. R., R. A. King, W. T. Forrester, D. L. Gallagher, A. L. Broadfoot, and C. C. Curtis (2001), Initial results from the IMAGE Extreme Ultraviolet Imager, *Geophys. Res. Lett.*, *28*(8), 1439.
Sandel, B. R., J. Goldstein, D. L. Gallagher, and M. Spasojevic (2003), Extreme ultraviolet imager observations of the structure and dynamics of the plasmasphere, *Space Sci. Rev.*, *109*, 25.
Sckopke, N. (1966), A general relation between the energy of trapped particles and the disturbance field near the Earth, *J. Geophys. Res.*, *71*, 3125.
Smith, C. W., M. H. Acuña, L. F. Burlaga, J. L'Heureux, N. F. Ness, and J. Scheifele (1998), The ACE magnetic fields experiment, *Space Sci. Rev.*, *86*, 613–632.
Southwood, D. J., and R. A. Wolf (1978), An assessment of the role of precipitation in magnetospheric convection, *J. Geophys. Res.*, *83*, 5227.
Stern, D. P. (1975), The motion of a proton in the equatorial magnetosphere, *J. Geophys. Res.*, *80*, 595.
Su, Y.-J., J. E. Borovsky, M. F. Thomsen, R. C. Elphic, and D. J. McComas (2000), Plasmaspheric material at the reconnecting magnetopause, *J. Geophys. Res.*, *105*, 7591.
Su, Y.-J., M. F. Thomsen, J. E. Borovsky, and D. J. Lawrence (2001), A comprehensive survey of plasmasphere refilling at geosynchronous orbit, *J. Geophys. Res.*, *106*, 25,615.
Summers, D., R. M. Thorne, and F. Xiao (1998), Relativistic theory of wave-particle resonant diffusion with application to electron acceleration in the magnetosphere, *J. Geophys. Res.*, *103*, 20,487.
Thomsen, M. F. (2004), Why Kp is such a good measure of magnetospheric convection, *Space Weather*, *2*, S11004, doi:10.1029/2004SW000089.
Thomsen, M. F., E. Noveroske, J. E. Borovsky, and D. J. McComas (1999), Calculation of moments from measurements by the Los Alamos magnetospheric plasma analyzer, *LA Rep. LA-13566-MS*, Los Alamos Natl. Lab., Los Alamos, N. M.
Thorne, R. M., E. J. Smith, R. K. Burton, and R. E. Holzer (1973), Plasmaspheric hiss, *J. Geophys. Res.*, *78*, 1581.
Tsyganenko, N. A. (2002), A model of the near magnetosphere with a dawn-dusk asymmetry: 2. Parameterization and fitting to observations, *J. Geophys. Res.*, *107*(A8), 1176, doi:10.1029/2001JA000220.
Tsyganenko, N. A., H. J. Singer, and J. C. Kasper (2003), Storm-time distortion of the inner magnetosphere: How severe can it get?, *J. Geophys. Res.*, *108*(A5), 1209, doi:10.1029/2002JA009808.
Volland, H. (1973), A semiempirical model of large-scale magnetospheric electric fields, *J. Geophys. Res.*, *78*, 171.
Weimer, D. R. (1996), A flexible, IMF dependent model of high-latitude electric potentials having "space weather" applications, *Geophys. Res. Lett.*, *23*, 2549.
Weimer, D. R. (2001), An improved model of ionospheric electric potentials including substorm perturbations and application to the Geospace Environment Modeling November 24, 1996, event, *J. Geophys. Res.*, *106*, 407.
Weiss, L. A., R. L. Lambour, R. C. Elphic, and M. F. Thomsen (1997), Study of plasmaspheric evolution during geosynchronous observed and global modeling, *Geophys. Res. Lett.*, *24*, 599.
Yeh, H.-C., J. C. Foster, F. J. Rich, and W. Swider (1991), Storm time electric field penetration observed at midlatitude, *J. Geophys. Res.*, *96*, 5707.
Young, D. T., H. Balsiger, and J. Geiss (1982), Correlations of magnetospheric ion composition with geomagnetic and solar activity, *J. Geophys. Res.*, *87*, 9077.
Zaharia, S., M. F. Thomsen, J. Birn, M. H. Denton, V. K. Jordanova, and C. Z. Cheng (2005), Effect of storm-time plasma pressure on the magnetic field in the inner magnetosphere, *Geophys. Res. Lett.*, *32*, L03102, doi:10.1029/2004GL021491.
Zaharia, S., V. K. Jordanova, M. F. Thomsen, and G. D. Reeves (2006), Self-consistent modeling of magnetic fields and plasmas of the inner magnetosphere: Application to a geomagnetic storm, *J. Geophys. Res.*, *111*, A11S14, doi:10.1029/2006JA011619.
Zhang, J.-C., M. W. Liemohn, M. F. Thomsen, and J. U. Kozyra (2006), A statistical comparison of solar wind driving of the plasma sheet during moderate and intense geomagnetic storms at solar minimum and maximum, *J. Geophys. Res.*, *111*, A07206, doi:10.1029/2005JA011559.

P. C. Brandt, Johns Hopkins University Applied Physics Laboratory, Laurel, MD, USA.
M. H. Denton, University of Southampton, Southampton, UK.
D. L. Gallagher, National Space Science and Technology Center, NASA Marshall Space Flight Center, Huntsville, AL, USA.
J. Goldstein, Southwest Research Institute, San Antonio, TX, USA.
M. G. Henderson and M. F. Thomsen, ISR-1, Los Alamos National Laboratory, Los Alamos, NM, USA.
J. U. Kozyra, M. W. Liemohn, and A. J. Ridley, Atmospheric, Oceanic, and Space Sciences Department, University of Michigan, 2455 Hayward Street, Ann Arbor, MI 48109-2143, USA. (liemohn@umich.edu)